Monthly Notices
of the
ROYAL ASTRONOMICAL SOCIETY

MNRAS **459,** 3635–3658 (2016)
Advance Access publication 2016 April 17

doi:10.1093/mnras/stw895

Properties of GRB light curves from magnetic reconnection

Paz Beniamini[1]★ and Jonathan Granot[2]

[1]*Racah Institute for Physics, The Hebrew University, Jerusalem 91904, Israel*
[2]*Department of Natural Sciences, The Open University of Israel, 1 University Road, PO Box 808, Ra'anana 4353701, Israel*

Accepted 2016 April 13. Received 2016 April 13; in original form 2015 September 7

ABSTRACT

The energy dissipation mechanism within gamma-ray burst (GRB) outflows, driving their extremely luminous prompt γ-ray emission is still uncertain. The leading candidates are internal shocks and magnetic reconnection. While the emission from internal shocks has been extensively studied, that from reconnection still has few quantitative predictions. We study the expected prompt-GRB emission from magnetic reconnection and compare its temporal and spectral properties to observations. The main difference from internal shocks is that for reconnection one expects relativistic bulk motions with Lorentz factors $\Gamma' \gtrsim$ a few in the jet's bulk frame. We consider such motions of the emitting material in two antiparallel directions (e.g. of the reconnecting magnetic-field lines) within an ultrarelativistic (with $\Gamma \gg 1$) thin spherical reconnection layer. The emission's relativistic beaming in the jet's frame greatly affects the light curves. For emission at radii $R_0 < R < R_0 + \Delta R$ (with $\Gamma = \text{const}$), the observed pulse width is $\Delta T \sim (R_0/2c\Gamma^2)\max(1/\Gamma', \Delta R/R_0)$, i.e. up to $\sim\Gamma'$ times shorter than for isotropic emission in the jet's frame. We consider two possible magnetic reconnection modes: a quasi-steady state with continuous plasma flow into and out of the reconnection layer, and sporadic reconnection in relativistic turbulence that produces relativistic plasmoids. Both of these modes can account for many observed prompt-GRB properties: variability, pulse asymmetry, the very rapid declines at their end and pulse evolutions that are either hard to soft (for $\Gamma' \lesssim 2$) or intensity tracking (for $\Gamma' > 2$). However, the relativistic turbulence mode is more likely to be relevant for the prompt sub-MeV emission and can naturally account also for the peak luminosity – peak frequency correlation.

Key words: magnetic reconnection – radiation mechanisms: non-thermal – gamma-rays: general.

1 INTRODUCTION

Gamma-ray bursts (GRBs) are the most extreme explosions in nature. They are powered by ultrarelativistic jets (with Lorentz factors $\Gamma \gtrsim 100$) and have huge isotropic equivalent luminosities ($L_{\rm iso} \approx 10^{53}$ erg s^{-1}). A good part of the outflow energy is thought to be dissipated at large distances ($R \sim 10^{13}$–10^{17} cm) from the central engine, where it efficiently radiates, predominantly in γ-rays that escape the emission region and eventually reach us. One of the major open questions in GRB research concerns the outflow composition. In particular, whether the energy is carried out from the central source to the emission region predominantly as kinetic energy – a baryonic jet (Shemi & Piran 1990), or as Poynting flux – a highly magnetized (or Poynting flux dominated) jet (Usov 1992; Thompson 1994; Mészáros & Rees 1997; Lyutikov & Blandford 2003; Granot et al. 2015). Recently, Beniamini & Piran (2014) have shown that the question of outflow composition is essentially tied to another major open question in GRB research – the nature of the prompt emission mechanism. In particular, one zone emission models in magnetic jets naturally produce efficient synchrotron radiation and predict fluxes in the X-ray and optical bands in excess of the observed ones during the prompt. However, the magnetization might still be high up until the emission region, and then sharply drop within the emission region itself (Drenkhahn & Spruit 2002; Lyutikov & Blandford 2003; Sironi, Petropoulou & Giannios 2015), if the dissipation that causes the emission is driven by efficient magnetic reconnection.

Magnetic jets can be powered by the rotational energy (ultimately arising from gravitational energy) of a magnetized torus around the black hole (Mészáros & Rees 1997) or of a highly magnetized millisecond neutron star (Usov 1992; Spruit 1999). Initially highly magnetized jets are favoured on energetic grounds, as modelling of GRB central engines that rely on accretion discs suggest that their power is significantly larger than that of thermally driven outflows powered by neutrino–antineutrino annihilation (see e.g. Kawanaka,

★ E-mail: paz.beniamini@mail.huji.ac.il

Piran & Krolik 2013). Moreover, a high value of the magnetization parameter σ (the magnetic to particle enthalpy density or energy flux ratio) near the source can help prevent excessive baryon loading that may prevent the jet from reaching sufficiently high Lorentz factors far from the source, at the emission region. Such initially highly magnetized jets may naturally lead to magnetic reconnection. In a striped wind magnetic field configuration (Coroniti 1990), with either periodic or stochastic flipping of the magnetic field direction near the source, reconnection at large distances from the source has a natural preferred direction. Moreover, for large σ-values just before the dissipation region, reconnection will lead to local relativistic bulk motion of the outgoing particles away from the reconnection sites (in the bulk frame of the jet). Therefore, reconnection models may be able to overcome the difficulties present in an isotropic arrangement of the magnetic fields regarding overproduction of optical and X-ray radiation (as compared with observations) due to synchrotron emission.

As mentioned above, synchrotron is likely the dominant source of emission in magnetic jets. Many studies have considered the implications of synchrotron radiation being the source of the prompt emission in GRBs (Katz 1994; Rees & Mészáros 1994; Sari, Narayan & Piran 1996; Sari, Piran & Narayan 1998; Kumar & McMahon 2008; Daigne, Bosnjak & Dubus 2011; Beniamini & Piran 2013). One of the greatest challenges for reconciling this model with the observations is related to the low-energy spectral slope. The synchrotron fast cooling (which is the likely cooling regime in order to achieve the required large radiative efficiencies) photon index below the peak, $\mathrm{d}N/\mathrm{d}E \propto E^{\alpha_\mathrm{B}}$ with $\alpha_\mathrm{B} = -1.5$, is inconsistent with the average observed slope of $\alpha_\mathrm{B} = -1$. Although it may be possible to achieve softer spectra, $\alpha_\mathrm{B} < -1.5$ (for instance by having the peak frequency fluctuate on a shorter time-scale than that for which the spectra are obtained, and in effect smearing the transition from below to above the synchrotron peak), it is not at all trivial to increase α_B in these models. However, 90 per cent of all GRB have $\alpha > -1.5$ (Preece et al. 2000; Ghirlanda, Celotti & Ghisellini 2002; Kaneko et al. 2006; Nava et al. 2011). In about 40 per cent of the GRBs $\alpha > -2/3$ (Nava et al. 2011), which is impossible for synchrotron, even in the case of slow cooling. This problem is known as the synchrotron 'line of death' (Preece et al. 1998b). However, a refined time-dependent spectral analysis in several bright bursts (Guiriec 2012) has suggested that GRB spectra may be better fitted with a multi-component model instead of the classical 'Band function'. In this model, the Band function component dominates the total energy but is accompanied by weaker power-law and blackbody components. The lower energy spectral slope of the Band function is softer than in Band only fits, and is consistent with slow cooling synchrotron (i.e. the synchrotron 'slow cooling line of death' problem is removed). Reconnection models may naturally allow for continuous heating of the electrons while they are emitting, in this way producing low-energy spectral slopes consistent with slow cooling while maintaining large radiative efficiencies (Ghisellini & Celotti 1999; Kumar & McMahon 2008; Fan 2010; Beniamini & Piran 2014).

An anisotropic emission model has been suggested to operate in the afterglow phase of GRBs (Beloborodov et al. 2011). These authors argued that synchrotron radiation is almost certainly anisotropic, and suggested that this anisotropy could help explain highly variable signals observed in some X-ray afterglows (such as the rapid decay phase or X-ray flares). In this work, we explore an analytic model in which the emitting electrons are anisotropic in the jet's bulk frame representing the bulk motion of the jet, or more specifically, are isotropic in their local centre of momentum (CM) frame, which moves relativistically relative to the jet's bulk frame. This could be applicable to reconnection from a striped wind where each pulse in the light curve of the prompt emission is due to some macroscopic reconnection event (Kumar & Crumley 2015). Moreover, it can also be applied in a broader context of anisotropic emission, such as had been suggested in the 'jet in jet' model (Levinson & Eichler 1993; Pedersen et al. 1998a; Frail et al. 2000) and the relativistic turbulence models (Lyutikov & Blandford 2003; Kumar & Narayan 2009; Lazar, Nakar & Piran 2009).

The paper is organized as follows. In Section 2, we present two different physical scenarios that can allow for anisotropic emission from reconnection zones. We discuss their different characteristics and present a simple argument, which shows that in contrast to 'non-boosted' reconnection models (i.e. the case where the particles' velocities are not strongly anisotropic in the jet frame), anisotropic models can be consistent with the observed variability in GRB light curves. Section 3 is devoted to a detailed description of the model that is considered in this work. Next, in Section 4 analytic expressions are derived for the resulting light curves, and their dependence on the model parameters is discussed. Section 5 features an extensive comparison of our results to GRB observations. Finally, our main results are summarized and discussed in Section 6.

2 MOTIVATION

2.1 The basic setup for relativistic magnetic reconnection

In GRBs and other relativistic outflow sources, magnetic reconnection is considered to be potentially most relevant if the outflow is initially Poynting flux dominated. In this case, magnetic reconnection is expected to be most efficient and prominent if a high σ is maintained in the outflow out to the reconnection site, so that the plasma that is inflowing into the reconnection region (or layer) is highly magnetized, with $\sigma \gg 1$. Such a situation is referred to as relativistic reconnection, as the total energy largely exceeds the rest energy of the particles and the outflow from the reconnection region is expected to be relativistic. For such relativistic magnetic reconnection, two main different types of reconnection models have been discussed in the literature.

The first type involves quasi-steady-state reconnection configurations with a continuous inflow of magnetized plasma into the reconnection layer, and a continuous outflow out of it. Analytic models of relativistic magnetic reconnection (in which the inflowing plasma is highly magnetized with $\sigma \gg 1$; e.g. Lyubarsky 2005) assume a single velocity for the plasma outflowing from the reconnection region, which they find to be relativistic (corresponding to a Lorentz factor of $\Gamma' \sim \sigma^{1/2} \gg 1$), and do not distinguish between individual particles of different energy. Particle In Cell (PIC) simulations (e.g. Cerutti et al. 2012, 2013; Guo et al. 2014; Melzani et al. 2014; Sironi & Spitkovsky 2014; Kagan et al. 2015), on the other hand, find that electrons that are accelerated to higher energies also spend a longer time being accelerated in the electric field within the reconnection layer, near the x-points, and thus their velocities become more tightly collimated. This leads to a positive correlation between the random Lorentz factor of the electrons γ'_e and their bulk Lorentz factor relative to the jet frame, Γ'. Moreover, once the electrons are deflected out of the x-point they quickly enter magnetic islands where their velocities are isotropized over their Larmour gyration time. Therefore, only electrons that emit a good fraction of their radiation within less than their Larmour gyration time will produce highly beamed radiation in the jet's bulk frame. This corresponds to emitted photon energies above the

synchrotron burn-off limit ($\gtrsim$100 MeV in the jet's bulk frame), which is also known as the 'maximum synchrotron energy' (de Jager et al. 1996) and corresponds to an observed energy of $h\nu_{\rm syn,\,max} = E_{\rm syn,\,max} \approx 7(1+z)^{-1}(\Gamma/100)$ GeV. Such high-energy electrons near the burn-off limit are highly 'fast cooling'. We stress that this set-up is therefore likely less relevant for explaining properties of the $\lesssim$MeV prompt emission. Within this model, the low-energy part of the spectrum is likely to be produced by non-boosted synchrotron emission in the jet's frame. Since the same electrons are producing both anisotropic and non-boosted emissions, the spectrum is expected to transition smoothly from the former to the latter, as the observed frequency decreases. Various implications of this scenario (at higher frequencies) are considered in detail in Section 4.5.

In this picture, in the vicinity of the x-points where $E^2 > B^2$ the electric field cannot vanish in any rest frame, and the particles are directly accelerated in the electric field. In the magnetic islands $E^2 < B^2$ and the particle velocities have been isotropized such that the CM particle velocity $\boldsymbol{\beta}'_{\rm CM}$ is the same for particles of all energies, so that in this plasma's rest frame, the charged particles can short-out the electric field, causing it to practically vanish (and thus approaching the ideal-MHD limit within the magnetic islands). As the velocity of the islands relative to the jet's bulk rest frame is small ($\beta'_{\rm isl} \ll 1$), the electric field in the jet's bulk frame is also very small there ($E'/B' \sim \beta'_{\rm isl} \ll 1$). This may be assumed to still hold to zeroth order also in the intermediate region between the x-points and the magnetic islands, where most of the beamed radiation is expected to be emitted. In this region one already has $E^2 < B^2$, but the particle velocities are still highly anisotropic and the particle CM velocity is energy dependent, $\boldsymbol{\beta}'_{\rm CM} = \boldsymbol{\beta}'_{\rm CM}(\gamma'_e)$, so that anyway the electric field could at most vanish in the CM frame of particles of one particular energy but not in that of particles of all other energies.

The second type of relativistic magnetic reconnection models invoke relativistic turbulence (Lyutikov & Blandford 2003; Kumar & Narayan 2009; Lazar et al. 2009; Inoue, Asano & Ioka 2011; Zrake 2014, 2015; East et al. 2015; Lazarian et al. 2015; Zrake & East 2016). In the context of GRBs within this type of model, different regions of the jet undergo sporadic reconnection events that give rise to relativistic bulk motions of plasma – 'blobs' or 'plasmoids' – relative to the jet's frame. In this picture, each blob is macroscopic and signifies a relativistic bulk motion relative to the jet's frame, where the blob's bulk velocity is equal to $\boldsymbol{\beta}'_{\rm CM}(\gamma'_{\rm e})$ for electrons of any $\gamma'_{\rm e}$.

Notice that although many plasmoids are found to be generated also in recent PIC simulations (Sironi & Spitkovsky 2014; Sironi et al. 2015), this structure is continuously evolving in time, as the magnetic islands merge with each other and grow larger and larger. This situation could then lead to an evolution of the spectrum within the prompt phase that is not observed. However, if the emission from all of the magnetic islands composing each reconnection layer produces a single spike in the light curve then it would predict spectral evolution within a single spike, which is observed. Moreover, since the increase in islands' sizes during this evolution is roughly linear, this would also imply that the acceleration time-scale of the highest energy electrons is dominated by the growth time of the largest island, which might explain the late onset of the high-energy emission (compared to the $\lesssim$MeV emission) in most bright *Fermi*/LAT GRBs (e.g. Abdo et al. 2009a,b; Ackermann et al. 2010). However, in this picture during a significant fraction of the pulse's dynamical time, it is no longer possible to maintain $t_{\rm acc} \ll t_{\rm dyn}$ as required in order to have continuous heating that balances the radiative cooling in order to avoid excess optical and X-ray emissions. Furthermore, recent studies (Melzani et al. 2014) find that the plasmoids generated in this setup are not necessarily travelling relativistically with respect to the jet's bulk frame. A blob-like emission described by the $k = 0$ mode is, however, observed in numerical studies involving relativistic turbulence. In this case, the turbulence can enhance the reconnection rate (e.g. Lazarian et al. 2015; Zrake 2015).

Ideal MHD holds within each blob and the electric field within its volume vanishes in its own frame. The electrons maintain a roughly isotropic velocity distribution within the blob's rest frame and their emission is approximately isotropic in this frame. Hence, the blob's emission is beamed in the jet's rest frame because of the blobs relativistic motion in this frame. Previous studies have focused on turbulence that is isotropic in the jet's frame. However, given an initially striped wind configuration of the magnetic field, it is likely that this turbulence would be largely constrained to a thin layer parallel to the shell front. Such an anisotropic relativistic turbulence would result in a correspondingly anisotropic emission in the jet's frame.

In this scenario, the electrons may be slow cooling. Moreover, second-order *Fermi* acceleration within the turbulent region can continuously heat the electrons until they reach a balance between heating and cooling (e.g. Murase et al. 2012; Asano & Terasawa 2015). This naturally allows for the electrons to remain hot while radiating, which is necessary in order to explain the observed prompt spectra from GRBs in a magnetically dominated emitting region (Beniamini & Piran 2014). In addition, boosted emission is necessary in order to explain the observed prompt variability as will be shown below. For these reasons, in this work we focus mainly on this second scenario, while the first scenario is addressed mainly in Section 4.5.

Finally, we remark that although the $k = 0$ and 1 models involve different modes of reconnection, they both rely on a similar initial physical set-up: a magnetically dominated jet, where each pulse in the light curve is produced by some macroscopic reconnection event in a layer perpendicular to the jet's propagation direction. While the $k = 0$ is more likely for explaining the observed properties of the sub-MeV pulse, it is possible that in at least some GRBs, the $k = 1$ mode is responsible for producing the GeV emission. In this case, the two modes may be operating in the same outflow. This may occur, for instance, if the initially quasi-steady state eventually drives turbulent reconnection until the later becomes the dominant mode of reconnection (see Lazarian et al. 2015). The ratio between the GeV emission and the sub-MeV pulse would depend in this case on the fraction of the flow involved in each reconnection mode and on their respective durations. Whether or not this can reproduce the observed ratio of these spectral components could be a potential test for this scenario.

2.2 Light-curve variability

In a simple, non-boosted emission picture, the reconnection model cannot easily reproduce the observed variability. This is because in order to obtain large-scale ordered reconnection, the speed of the incoming plasma that approaches the reconnection region from both sides is expected to be $v'_{\rm in} = \beta'_{\rm in}c \lesssim 0.1{-}0.25c$ (Lyubarsky 2005; Guo et al. 2015; Liu et al. 2015). Therefore, if the radial width of the region feeding the reconnection layer is L in the lab frame and $L' = \Gamma L$ in the jet's bulk frame, then the reconnection lasts $\Delta t' = L'/v'_{\rm in}$ in the jet's bulk frame, and $\Delta t = \Gamma \Delta t'$ in the lab frame. The time over which the radiation that emitted from this reconnection event along the line of sight reaches the observer, or the radial time of the resulting pulse, is $\Delta T_{\rm r} = (1-\beta)\Delta t \approx L/2v'_{\rm in}$.

The increase in radius during the reconnection event is $\Delta R \approx c\Delta t$, and since this is a lower limit to the emission radius, $R \geq \Delta R$, the angular spreading time in the arrival of photons to the observer, which is a lower limit to the pulse width, is at least

$$\Delta T_\theta = \frac{R}{2c\Gamma^2} \geq \frac{\Delta R}{2c\Gamma^2} \approx \frac{L}{2v'_{\rm in}} \approx \Delta T_{\rm r}. \quad (1)$$

The total pulse width accounts for both radial and angular spreading in the photon arrival times, and is therefore

$$\Delta T \sim \Delta T_{\rm r} + \Delta T_\theta \sim \frac{L}{v'_{\rm in}}. \quad (2)$$

This is a factor of $\sim 10(\beta'_{\rm in}/0.1)^{-1}$ larger than the difference in the ejection time of neighbouring reconnecting layers or shells, $\Delta t_{\rm ej} \approx L/c$, which would also be the difference in the onset times of neighbouring pulses for emission from the same radius. While fluctuations are possible around this typical difference in pulse onset times, the mean separation does not vary unless the emission radius systematically changes throughout the GRB. There is, however, observational evidence against this, since the gross properties of the GRB emission do not appear to systematically change throughout the prompt emission.

The time between pulses can increase if only a small portion of the jet material would have contributed to the observed radiation (i.e. if the distance between the reconnection layers is larger than L, so that $\Delta t_{\rm ej}$ would be correspondingly larger, where the added outflow layer does not contribute to the reconnection). However, assuming a roughly constant jet power this would imply that only a correspondingly small fraction is dissipated and contributes to the γ-ray emission. This is because significant pressure gradients tend to be washed out, so that a smooth pressure profile may be expected in the propagation direction. For a fixed local bulk Lorentz factor the energy flux is proportional to the proper enthalpy density, $w + B^2/4\pi = w(1+\sigma)$, which in the highly magnetized regions ($\sigma \gg 1$) is dominated by the magnetic term, half of which arises from the magnetic pressure $B^2/8\pi$. The thermal pressure, on the other hand, can account for at most one quarter of the particle proper enthalpy density, $w = \rho c^2 + e_{\rm int} + p$, since even for a relativistically hot plasma $p = e_{\rm int}/3 \approx w/4$. Therefore, a comparable energy per unit length in the propagation direction is expected also for low magnetization regions ($\sigma < 1$) or highly magnetized regions that do not border an oppositely oriented magnetic field region with which they can easily reconnect (e.g. if the field orientation changes randomly due to fluctuations in an accretion disc around a black hole, rather than very orderly as in a strong MHD wind launched by a newly born millisecond magnetar). This could be very challenging for the total energy budget of the GRB, as the total jet energy would be even larger than current in estimates, which are already considered highly demanding for viable GRB progenitors (Panaitescu & Kumar 2002; Fan & Piran 2006; Granot, Konigl & Piran 2006; Beniamini et al. 2015).

All this implies that the 'simple' reconnection model predicts pulses that are significantly broader than the intervals between them, contrary to what is seen in observations (see also Lazar et al. 2009), namely that these times are roughly equal (Nakar & Piran 2002). Therefore, it is interesting to explore a slightly more complicated yet physically motivated reconnection model, which may be able to both account for the continuous heating, as well as reproduce the observed variability. In this model, the plasma in the thin reconnection region is ejected away from the X-point along the reconnection layer at a relativistic speed in the jet's bulk frame, corresponding to a Lorentz factor Γ'. The emission is assumed to be isotropic in a frame moving at Γ' relative to the jet's bulk frame, and is therefore anisotropic in the jet's bulk frame for $\Gamma' \gg 1$.

Anisotropic emission in the jet's bulk frame only reduces ΔT_θ by a factor of $\sim\Gamma'$, while it does not change $\Delta T_{\rm r}$. Therefore, given that $\Delta T \sim \Delta T_{\rm r} + \Delta T_\theta$, for a smooth continuous emission as a function of radius (and $\Gamma' \gtrsim$ a few) $\Delta T \sim \Delta T_{\rm r} \sim R/2c\Gamma^2 \approx \Delta t_{\rm ej}/2\beta'_{\rm in} = 5(\beta'_{\rm in}/0.1)^{-1}\Delta t_{\rm ej}$. However, since $\Delta T_\theta \sim \Delta T_{\rm r}/\Gamma'$ is significantly smaller than $\Delta T \sim \Delta T_{\rm r}$, and the emission at any given radius originates from a small part (a fraction $\sim 1/(\Gamma')^2$) of the visible region (corresponding to angles $\theta \lesssim 1/\Gamma$ from the line of sight), variations in the emission intensity with radius would be reflected in the light curve down to the shorter angular time-scale $\Delta T_{\rm r}/\Gamma'$. Moreover, such variations are arguably quite likely in efficient (high σ) magnetic reconnection (i.e. reconnection leading to dissipation of a significant fraction of the total energy), which is rarely very smooth and continuous. Therefore, it is likely to typically observe variability on the shorter angular time-scale $\Delta T_{\rm r}/\Gamma'$.

One implication of this model is that it naturally results in larger emitting radii than those usually implied from the variability time-scale. This is because for non-boosted emission in the jet's bulk frame the observed variability time-scale is given by

$$\Delta T_{\rm iso} = \frac{R_{\rm iso}}{2c\Gamma^2}, \quad (3)$$

whereas in the current model it is shorter by a factor of $\sim\Gamma'$, $\Delta T \sim \Delta T_{\rm iso}/\Gamma'$. This would imply a larger emission radius in order to reproduce the same observed variability time-scales. For $\Gamma \approx 300$, $\Gamma' \approx 10$ and $\Delta T = 1$ s we obtain $R \approx 5 \times 10^{16}$cm. This radius is 10 times larger than would be inferred for a non-boosted emission in the jet's bulk frame, and is still a few times smaller than typical estimates for the deceleration radius (and therefore consistent with the interpretation that the prompt signal originates at R).

3 THE MODEL

3.1 The physical model

We associate each pulse in the light curve with emission from a different thin 'shell'. In the context of a striped wind each 'shell' is associated with the thin reconnection layer between regions (wider spherical shells) of oppositely oriented tangential (primarily toroidal) magnetic field lines. In this section, we discuss the emission from a single shell, and in Section 4.6 we show that adding up the emission from many shells produce light-curve variability similar to that seen in observations.

Consider an ultrarelativistic (moving with $\Gamma \gg 1$ in the rest frame of the central source) thin [of radial width $\ll R/(\Gamma^2\Gamma')$] 'spherical' (occupying an angle θ around the line of sight such that $\theta\Gamma \gtrsim$ a few) shell which starts emitting at some initial radius R_0 (possibly, but not necessarily due to reconnection) and turns off at a final radius $R_{\rm f} \geq R_0$. Let the emitters be moving with a Lorentz factor Γ' in the local bulk frame of the flow, in two opposite directions that are perpendicular to the radial direction. There are three relevant frames in this paper: (i) the central source frame, (ii) the jet's local bulk frame, which moves with a Lorentz factor Γ in the radial direction to the central source, and (iii) the emitters' frame which moves with a Lorentz factor Γ' compared to the jet's bulk frame, in which the radiation is assumed to be emitted isotropically. Quantities in frame (i) are un-primed, those in frame (ii) are primed, while quantities in frame (iii) are double primed. With these definitions, the emitters' speed is given by $\boldsymbol{\beta'} = \pm\beta'\hat{x}'$ ($\hat{z}' = \hat{r}$ is the radial direction in the jet's bulk frame). $\hat{x}'$ is the projection of $\hat{x}$ (the direction

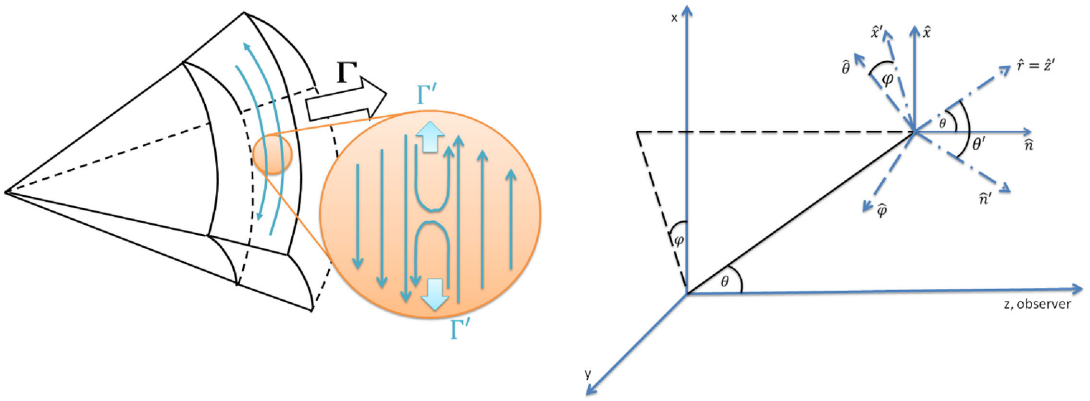

Figure 1. Left: schematic geometry of the model at hand. The emitting matter is moving relativistically out of the reconnection x-points at a Lorentz factor Γ' in the jet's bulk frame (i.e. relative to the bulk of the outflow). Right: the two reference frames used in this work: the lab frame with the origin at the central source (in either Cartesian or spherical coordinates), and the jet's bulk frame (denoted by primes), travelling at a Lorentz factor Γ in the $\hat{r} = \hat{z}'$ direction and centred at the emission point.

perpendicular to the direction to the observer $\hat{n} = \hat{z}$) on the plane perpendicular to the radial direction. Notice that: $\hat{n}' = \hat{r}\cos\theta' - \hat{\theta}\sin\theta'$. In addition:

$$\hat{x}' = \frac{(\hat{\theta}\cdot\hat{x})\hat{\theta} + (\hat{\phi}\cdot\hat{x})\hat{\phi}}{\sqrt{(\hat{\theta}\cdot\hat{x})^2 + (\hat{\phi}\cdot\hat{x})^2}} = \frac{\hat{\theta}\cos\theta\cos\phi - \hat{\phi}\sin\phi}{\sqrt{\sin^2\phi + \cos^2\theta\cos^2\phi}}$$
$$= \frac{\hat{\theta}\cos\theta\cos\phi - \hat{\phi}\sin\phi}{\sqrt{1 - \sin^2\theta\cos^2\phi}} \approx \hat{\theta}\cos\phi - \hat{\phi}\sin\phi\,, \tag{4}$$

where $\hat{\beta}' = \pm\hat{x}'$ and we have approximated $\cos^2\theta = 1 - \sin^2\theta \approx 1$. Moreover,

$$\cos\phi' = \hat{x}'\cdot\hat{\theta} = \frac{\cos\theta\cos\phi}{\sqrt{1 - \sin^2\theta\cos^2\phi}} \approx \cos\phi\,. \tag{5}$$

Combining this with the expression for $\hat{n}'$ we get that $\hat{n}'\cdot\hat{\beta}' = \pm\sin\theta'\cos\phi'$. For a schematic figure of the geometry see Fig. 1. We aim to find the resulting light curve in the observer's frame. Our modelling follows that of (Genet & Granot 2009, which relies on the formalism developed in Granot 2005; Granot, Cohen-Tanugi & do Couto e Silva 2008), and converges to the results in this paper in the limit of $\Gamma' \to 1$ (and $\beta' \to 0$), corresponding to the case of non-boosted emission. Notice that once the motion of the local CM velocity of the emitting particles becomes non-relativistic, their radiation is no longer beamed and even if they emit in a very ordered magnetic field, their emission pattern will be broadly similar to isotropic emission in the jet's bulk frame (Granot et al. 2002; Granot & Königl 2003; Beloborodov et al. 2011), and the situation reduces back to the simple 'one zone' case.

The jet may be accelerating, coasting or decelerating as it is emitting (see Section 6 for more details). To account for this, the Lorentz factor of the bulk is assumed to evolve as a power law with radius: $\Gamma^2 = \Gamma_0^2(R/R_0)^{-m}$ where $\Gamma_0 = \Gamma(R_0)$. The case of a coasting jet (with no acceleration or deceleration) can be easily obtained by setting $m = 0$ in the following equations. The luminosity is assumed to be isotropic in the emitter's frame (double primed frame) and depends only on the radius:

$$L''_{\nu''}(R) = L''_{\nu''_0} S[\nu''/\nu''_{\rm p}] f(R/R_0)\,. \tag{6}$$

In the last expression, $f(x)$ is a dimensionless function of the radius that is normalized such that $\int_0^\infty f(x){\rm d}x = 1$, $\nu''_{\rm p}$ is the frequency where $\nu'' L''_{\nu''}$ peaks, and $S(x)$ is the spectrum (which is assumed to be a Band function),

$$S(x) = {\rm e}^{2+\alpha_{\rm B}} \begin{cases} x^{1+\alpha_{\rm B}}{\rm e}^{-(2+\alpha_{\rm B})x} & x \leqslant x_b\,, \\ x^{1+\beta_{\rm B}} x_b^{\alpha_{\rm B}-\beta_{\rm B}}{\rm e}^{-(\alpha_{\rm B}-\beta_{\rm B})} & x \geqslant x_b\,, \end{cases} \tag{7}$$

where $x_b = (\alpha_{\rm B} - \beta_{\rm B})/(2 + \alpha_{\rm B})$, while $\alpha_{\rm B}$ and $\beta_{\rm B}$ are the high- and low-energy slopes of the spectrum. For $\alpha_{\rm B} > -2 > \beta_{\rm B}$, the Band function has a peak in the νF_ν spectrum, at $x = 1$, and therefore since $S(x)$ is normalized such that $S(x) = xS(x) = 1$ at $x = 1$, it will not affect normalization of νF_ν at its peak. The two functional forms used in the Band function are matched at $\nu''_b = x_b \nu''_p$.

The flux is then given by

$$F_\nu(T) = \frac{1}{4\pi D^2}\int {\rm d}L_\nu = \frac{1}{4\pi D^2}\int \mathcal{D}^3 {\rm d}L'_{\nu'}$$
$$= \frac{1}{4\pi D^2}\int \mathcal{D}^3 \frac{\mathcal{D}'^{3-k}}{\Gamma'^k}{\rm d}L''_{\nu''}\,, \tag{8}$$

where for convenience we denote the effective distance to the source in terms of the luminosity distance and redshift by $D = d_{\rm L}/\sqrt{1+z}$. In addition, $\mathcal{D}$ is the Doppler factor from the jet's bulk frame (the rest frame of the bulk) to the observer frame (the rest frame of the central source), $\mathcal{D}'$ is the Doppler factor from the emitter's frame to the jet's bulk frame and ${\rm d}L''_{\nu''} = L''_{\nu''}(R){\rm d}\mu{\rm d}\phi/(4\pi)$. In the last expression, $\mu = \cos\theta$ where θ is the angle between the emitting location and line of sight and ϕ is the azimuthal angle (these are the angles in a spherical coordinate system whose origin is at the central source while its z-axis points towards the observer). This implies that the observed frequency (ν) is related to the frequencies in the jet's bulk frame (ν') and in the emitter's frame (ν'') by $(1+z)\nu = \mathcal{D}\nu' = \mathcal{D}\mathcal{D}'\nu''$. The parameter k can obtain only two possible values: $k = 1$ in case each emitter produces continuous emission (a steady state in the jet's bulk frame, e.g. as in Section 4.5), or $k = 0$ in case the emitters produce a single 'blob' (as is likely for the turbulent scenario discussed in Section 2). The observed time T is set such that $T = 0$ corresponds to the arrival time of a photon emitted at the central source (i.e. in the origin) at the ejection time of the shell. The first photons to reach the observer from the emission at radii $R_0 \leq R \leq R_{\rm f}$ are from along the line of sight ($\theta = 0$) from $R = R_0$, and arrive (accounting for cosmological redshift) at

$$T_0 = \frac{(1+z)R_0}{2(m+1)c\Gamma_0^2}\,. \tag{9}$$

We define the equal arrival time surface (EATS) as the locus of points from which photons emitted at different radii R and angles θ relative to the line of sight, reach the observer simultaneously at an observed time T. The maximal radius along the EATS, $R_{\rm L}(T)$ (which is obtained along the line of sight), and the Lorentz factor at that radius, $\Gamma_{\rm L}(T)$, can be conveniently expressed in terms of this time,

$$\frac{R_{\rm L}}{R_0}=\left(\frac{T}{T_0}\right)^{1/m+1},\quad \frac{\Gamma_{\rm L}}{\Gamma_0}=\left(\frac{R_{\rm L}}{R_0}\right)^{-m/2}=\left(\frac{T}{T_0}\right)^{-m/2(m+1)}. \tag{10}$$

3.2 The observed flux

In order to calculate the flux density F_ν that reaches the observer at time T, we integrate the luminosity $L''_{\nu''}$ over the EATS. This introduces a relation between R and θ, $T/(1+z)=t-R\mu/c$, for photons arriving at a given time. In addition, since the emission in our model is anisotropic, photons emitted at different ϕ will have different Doppler factors from the emitter's frame to the bulk frame and we cannot use symmetry arguments to integrate over ϕ. As we assume $\Gamma\gg1$, because of relativistic beaming only angles of $\theta\Gamma\lesssim$ a few contribute significantly to the observed flux, so one can safely assume $\theta\ll1$. It is convenient to use the dimensionless normalized radius $y=R/R_{\rm L}$ and change variables of integration for calculating the flux from μ to y or $\mathrm{d}\mu\rightarrow|\mathrm{d}\mu/\mathrm{d}y|\mathrm{d}y$, using the relation

$$\left|\frac{\mathrm{d}\mu}{\mathrm{d}y}\right|=\frac{y^{-2}+my^{m-1}}{2(m+1)\Gamma_{\rm L}^2}=\left(\frac{T}{T_0}\right)^{m/m+1}\frac{1}{\Gamma_0^2}\frac{(m+y^{-m-1})y^{m-1}}{2(m+1)}. \tag{11}$$

The Doppler factors and can be expressed as

$$\mathcal{D}=\frac{1}{\Gamma(1-\beta\mu)}=\Gamma_{\rm L}\frac{2(m+1)y^{-m/2}}{m+y^{-m-1}}=\left(\frac{T}{T_0}\right)^{-m/2(m+1)}\Gamma_0\frac{2(m+1)y^{-m/2}}{m+y^{-m-1}}, \tag{12}$$

$$\mathcal{D}'=\frac{1}{\Gamma'(1-\beta'\sin\theta'\cos\phi')},$$

$$\sin\theta'=2\frac{\sqrt{(m+1)(y^{-m-1}-1)}}{m+y^{-m-1}}. \tag{13}$$

One can also define $\nu_0\equiv2\Gamma_0\Gamma'\nu''_0/(1+z)$ and use it in order to express

$$x=\frac{\nu''}{\nu''_p}=\frac{\nu}{\nu_0}\left(\frac{m+y^{-m-1}}{m+1}\right)\left(\frac{y}{y_{\rm min}}\right)^{m/2}\Gamma'^2(1-\beta'\sin\theta'\cos\phi), \tag{14}$$

where the limits of integration over y are from $y_{\rm min}=\min(1,R_0/R_{\rm L})$ to $y_{\rm max}=\min(1,R_{\rm f}/R_{\rm L})$.

A general expression for the flux is then given by

$$F_\nu(T)=\frac{2\Gamma_0\Gamma'L''_{\nu''_0}}{4\pi D^2}\left(\frac{T}{T_0}\right)^{-m/2(m+1)}\times\int_{y_{\rm min}}^{y_{\rm max}}\mathrm{d}y\left(\frac{m+1}{m+y^{-m-1}}\right)^2y^{-1-m/2}\,f\left[y\left(\frac{T}{T_0}\right)^{1/m+1}\right]\times\frac{1}{2\pi\Gamma'^4}\int_0^{2\pi}\mathrm{d}\phi\,(1-\beta'\sin\theta'\cos\phi)^{k-3}\,S[x(\phi,y)]. \tag{15}$$

4 RESULTS FOR SINGLE-PULSE EMISSION

We turn to a detailed discussion of the results of our model. In Sections 4.1 and 4.2, we present simple analytic expressions for the general flux provided in equation (15) for specific spectral and radial emission profiles. The light curves of single pulses under various assumptions are presented in Section 4.3. Their dependence on the radial width of the jet contributing to the emission and on the emitters' Lorentz factor, Γ', as well as estimates for their degree of asymmetry are taken up in Section 4.4. In Section 4.5, we deviate from the main model considered in the paper, and, motivated by PIC simulations, turn to a discussion of the predicted emission from a continuous injection of particles to the reconnection layer resulting in a correlation between the random Lorentz factor of the electrons and the bulk Lorentz factor of the emitters. The results derived under these assumptions are likely to be less relevant for explaining the properties of the sub-MeV pulse, but can still have interesting implications for the emission at very high frequencies. Finally in Section 4.6, we present the results for the entire light curve using different distributions of the intrinsic parameters of the model.

4.1 Analytic estimates for power-law spectra and power-law function in radius

For a power-law spectrum, $S_{\rm PL}(x)=x^{-\alpha}=(\nu''/\nu''_0)^{-\alpha}$, one can obtain a somewhat simpler analytic formula for the observed flux. In this case since $f(R/R_0)=0$ for $R<R_0$ (see below), one can effectively plug $y_{\rm min}=R/R_{\rm L}$ in equation (14) to obtain

$$x=\frac{\nu''}{\nu''_0}=\frac{\nu}{\nu_0}\left(\frac{T}{T_0}\right)^{m/2(m+1)}\times\left(\frac{m+y^{-m-1}}{m+1}\right)y^{m/2}\Gamma'^2(1-\beta'\sin\theta'\cos\phi). \tag{16}$$

Substituting $S(x)\rightarrow S_{\rm PL}(x)=x^{-\alpha}$ and:

$$f(R/R_0)=\begin{cases}\frac{(a+1)}{(R_{\rm f}/R_0)^{a+1}-1}(R/R_0)^a & R_0<R<R_{\rm f},\\ 0 & \text{otherwise},\end{cases} \tag{17}$$

in equation (15) yields

$$F_\nu(T)=\frac{2\Gamma_0\Gamma'L''_{\nu''_0}}{4\pi D^2}\left(\frac{\nu}{\nu_0}\right)^{-\alpha}\left(\frac{T}{T_0}\right)^{2a-m(1+\alpha)/2(m+1)}\times\frac{(a+1)}{\left(\frac{R_{\rm f}}{R_0}\right)^{a+1}-1}\int_{y_{\rm min}}^{y_{\rm max}}\mathrm{d}y\left(\frac{m+1}{m+y^{-m-1}}\right)^{2+\alpha}y^{a-1-m/2(1+\alpha)}\times\frac{1}{2\pi\Gamma'^{4+2\alpha}}\int_0^{2\pi}\mathrm{d}\phi\,(1-\beta'\sin\theta'\cos\phi)^{k-3-\alpha}. \tag{18}$$

It is easy to see that equation (18) reduces to equation (13) of Granot et al. (2008) for $\Gamma'=1$ (and without the attenuation term in that paper, due to γ–γ opacity). At the other extreme, $\Gamma'\gg1$, equation (18) can be approximately estimated (see Appendix A for a derivation) as

$$F_\nu(T)\approx\frac{\Gamma_0\Gamma'^{1-2k}L''_{\nu''_0}}{2^k\pi D^2}\left(\frac{\nu}{\nu_0}\right)^{-\alpha}\left(\frac{T}{T_0}\right)^{2a-m(1+\alpha)/2(m+1)}\times\frac{(a+1)(m+2)^{m(\alpha-1)-2(a+1)/2(m+1)}}{\left(1+\frac{\Delta R}{R_0}\right)^{a+1}-1}\frac{\Gamma(2+\alpha-k)}{\Gamma(3+\alpha-k)}. \tag{19}$$

We see that for a blob like emission ($k=0$), we obtain $F_\nu(T)\propto\Gamma'$ as expected from beaming. For continuous emission ($k=1$),

the flux appears to be suppressed by a factor Γ'^{-2}. This is because in continuous emission, the emission at each location in the jet's bulk frame remains constant in time as the emitting plasma flows through it, while for a single blob of plasma the location of the emission (i.e. of the blob) moves in the jet's bulk frame and chases after the photons it emits, and for the viewing angle from which it appears most luminous it trails them just by a small amount, so that the same emitted photons (over the same time interval in the jet's bulk frame) arrive to a stationary observer (in the jet's bulk frame, and also to us) over a shorter time interval (by a factor of $dt'_{\rm obs}/dt' = (\Gamma'\mathcal{D}')^{-1} = 1-\beta'\sin\theta'\cos\phi'$) compared to a steady, continuous flow, resulting in a flux larger by the inverse of this factor, $\Gamma'\mathcal{D}'$. Alternatively, a continuous flow can be approximated as composed of a large number of blobs, in which case only a fraction $(\Gamma'\mathcal{D}')^{-1}$, of the N blobs that are instantaneously within a given segment of the flow contribute to the observed emission (or photon front) from that segment, resulting in a flux smaller by this factor compared to a single blob with the combined luminosity of the N blobs. For the observed flux in our case, the viewing angle relative to the direction of the emitting fluid in the jet's bulk frame changes with time and between the different parts of the source, so that altogether the total flux reflect a weighted mean of $(\Gamma'\mathcal{D}')^{-1}$, which is $\sim\Gamma'^{-2}$, for the suppression factor of a continuous flow compared to a single blob. Stated differently, the total energy emitted in the two cases, scales as $E \propto L''_{\nu''}\Gamma'^{-2k}$, since in order to emit over the same observed duration, a blob needs to emit in its own rest frame over a time longer by a factor of $\sim\Gamma'^2$ with the same luminosity. This implies that in order to keep the total emitted energy constant in the two scenarios, we must change the luminosity in the emitters' frame according to: $L''_{\nu''} \propto \Gamma'^{2k}$. Plugging this back to equation (19), we obtain the expected scaling with Γ', independent of k.

4.2 Analytic estimates for power-law spectra and single emission radius

Another simple test-case is that of a power-law spectra (as in Section 4.1) but with a delta-function emission in radius,

$$f\left(\frac{R}{R_0}\right) = R_0\delta(R-R_0) = \delta\left(\frac{R}{R_0}-1\right) = \delta\left(\frac{y}{y_{\rm min}}-1\right) = y_{\rm min}\delta(y-y_{\rm min}), \quad (20)$$

where $y_{\rm min} = (T/T_0)^{-1/(m+1)}$. In this case, one can analytically perform the integral over y and obtain

$$F_\nu(T) = \frac{2\Gamma_0\Gamma' L''_{\nu''_0}}{4\pi D^2}\left(\frac{\nu}{\nu_0}\right)^{-\alpha}\left(\frac{m+1}{m+\frac{T}{T_0}}\right)^{2+\alpha} \times \frac{\Gamma'^{-4-2\alpha}}{2\pi}\int_0^{2\pi}{\rm d}\phi\left(1-2\beta'\frac{\sqrt{(m+1)\left(\frac{T}{T_0}-1\right)}}{m+\frac{T}{T_0}}\cos\phi\right)^{k-3-\alpha} \quad (21)$$

It is convenient to use here the initial radial time $T_0 = T_{\rm r}(R_0)$ given by equation (9), which is the time when the first photons reach the observer (for our definition of $T = 0$ as the arrival time of photons from the source when the shell is ejected), and the corresponding angular time, $T_\theta = T_\theta(R_0) = R_0/(2c\Gamma_0^2) = (m+1)T_{\rm r}(R_0) = (m+1)T_0$ that determines the width of the pulse. We also define $T_{\rm s} = T_0 - T_\theta = -mT_0$. We may now write the expression for the flux as

$$F_\nu(T) = \frac{2\Gamma_0\Gamma' L''_{\nu''_0}}{4\pi D^2}\left(\frac{\nu}{\nu_0}\right)^{-\alpha}\left(\frac{T-T_{\rm s}}{T_\theta}\right)^{-2-\alpha} \times \frac{\Gamma'^{-4-2\alpha}}{2\pi}\int_0^{2\pi}{\rm d}\phi\left(1-2\beta'\frac{\sqrt{(T-T_0)T_\theta}}{T-T_{\rm s}}\cos\phi\right)^{k-3-\alpha} \quad (22)$$

For $\beta' = 0$, the integrand becomes 1 and we obtain a power-law decay with a temporal index $2+\alpha$ as is well known for high latitude emission. At the other extreme, for $\beta' \to 1$ the integrand becomes maximal when $\sin\theta' = 2\sqrt{(m+1)\bar{T}}/(m+1+\bar{T}) \approx 1$ where $\bar{T} \equiv (T-T_0)/T_0$, which occurs for $\bar{T} \approx m+1$, and $\cos\phi \approx 1$, which occurs for $\phi \approx 0$. Therefore, the peak in the light curve occurs at small values of $\bar{t} \equiv [\bar{T}/(m+1)] - 1$, and for estimating the fluence (i.e. evaluating the light curve around its peak) we may assume that $\bar{t} \ll 1$, where in this limit $\sin\theta' \approx 1-\bar{t}^2/8$, and $(T-T_{\rm s})/T_\theta = (m+T/T_0)/(m+1) \approx 2$. In terms of ϕ, the width of the region where the dominant contribution comes from is roughly $\sim 1/\Gamma' \ll 1$ around $\phi = 0$ or $|\phi|\Gamma' \lesssim$ a few, so that we can safely assume $|\phi| \ll 1$, $\cos\phi \approx 1-\phi^2/2$, and take the limits of integration to be from $-\infty$ to ∞, where $1-\beta'\sin\theta'\cos\phi \approx [1+(\Gamma'\bar{t}/2)^2+(\Gamma'\phi)^2]/2\Gamma'^2 = (1+\tilde{t}^2+\tilde{\phi}^2)/2\Gamma'^2$ (where $\tilde{t} \equiv \Gamma'\bar{t}/2$ and $\tilde{\phi} \equiv \Gamma'\phi$),

$$\begin{aligned} F_\nu\left(\frac{T}{T_0} \approx m+2\right) &\approx \frac{2\Gamma_0\Gamma' L''_{\nu''_0}}{4\pi D^2}\left(\frac{\nu}{\nu_0}\right)^{-\alpha}\left(\frac{T-T_{\rm s}}{T_\theta}\right)^{-2-\alpha} \times\frac{\Gamma'^{-4-2\alpha}}{2\pi}\int_{-\infty}^{\infty}{\rm d}\phi\left(\frac{1+(\Gamma'\bar{t}/2)^2+(\Gamma'\phi)^2}{2\Gamma'^2}\right)^{k-3-\alpha} \\ &= \frac{\Gamma_0\Gamma'^{2-2k}L''_{\nu''_0}}{2^{k-1-\alpha}\pi^2 D^2}\left(\frac{\nu}{\nu_0}\right)^{-\alpha}\int_{-\infty}^{\infty}{\rm d}\tilde{\phi}\,(1+\tilde{t}^2+\tilde{\phi}^2)^{k-3-\alpha} \\ &= \frac{\Gamma_0\Gamma'^{2-2k}L''_{\nu''_0}}{2^{k-1-\alpha}\pi^{3/2}D^2}\left(\frac{\nu}{\nu_0}\right)^{-\alpha}\frac{\Gamma(2.5+\alpha-k)}{\Gamma(3+\alpha-k)}(1+\tilde{t}^2)^{k-5/2-\alpha}. \quad (23) \end{aligned}$$

We have $dT = (2T_\theta/\Gamma')d\tilde{t}$, and near the peak $F_\nu(\tilde{t}) \approx K(1+\tilde{t}^2)^{k-2.5-\alpha}$ so that the fluence is given by

$$\begin{aligned} f_\nu &= \int dT\,F_\nu(T) \approx \frac{2KT_\theta}{\Gamma'}\int_{-\infty}^{\infty}d\tilde{t}\,(1+\tilde{t}^2)^{k-5/2-\alpha} \\ &= \frac{\Gamma_0\Gamma'^{1-2k}L''_{\nu''_0}T_\theta}{2^{k-2-\alpha}\pi D^2}\left(\frac{\nu}{\nu_0}\right)^{-\alpha}\frac{\Gamma(2+\alpha-k)}{\Gamma(3+\alpha-k)}. \quad (24) \end{aligned}$$

The dependence on Γ_0 and Γ' in equation (24) is the same as in equation (19), while in equation (23) there is an extra power of Γ'. This arises since the width of the peak in the light curve for the emission from a single radius is $\sim T_\theta/\Gamma'$, i.e. $\sim 1/\Gamma' \ll 1$ times the angular time from that radius, due to the beaming of the emission in the jet's bulk frame. The time dependence of the emission near the peak, in equation (23) is dominated by the beaming in the jet's bulk frame, while at late times $T \gg T_\theta$ it becomes dominated by the usual high-latitude emission, as the beaming in the jet's bulk frame approaches a constant [i.e. the $\hat{n}' \approx -\hat{r}$ and the integral in equation (22) approaches a constant, leaving only the explicit time dependence in front of the integral]. While for $\Delta R = R_{\rm f} - R_0 \sim R_0$ the pulse width is $\sim T_\theta$, the normalization of the emission from a single radius is such that the fluence in both cases is similar.

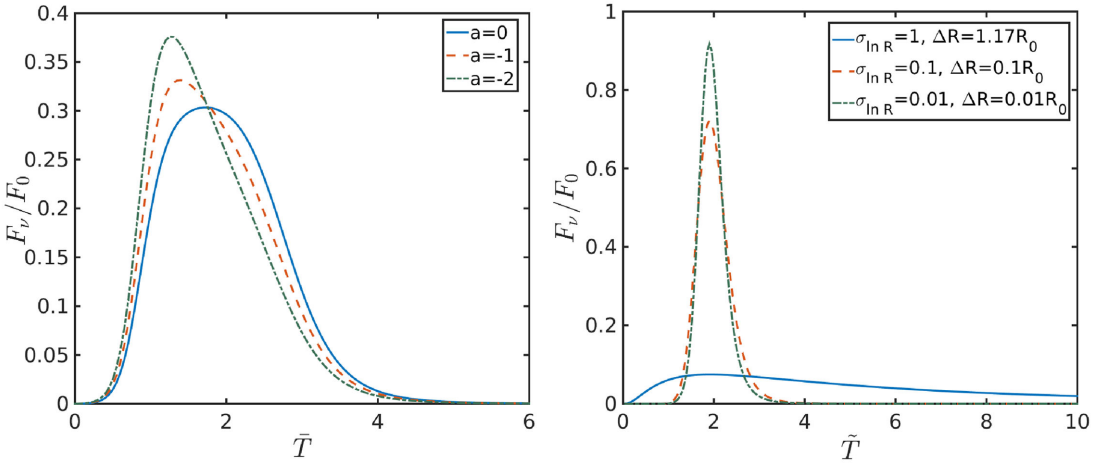

Figure 2. Light curves of a single pulse with a power law between R_0 and $R_f = 2R_0$ (left-hand panel) and lognormal (right-hand panel) dependence of the luminosity on radius. All cases are plotted for a typical Band function spectral emissivity and $\Gamma' = 3$, $m = 0$, $k = 0$. The flux is given in units of the 'typical' peak flux F_0 (giving in equation 26), and shown as a function of the normalized time $\bar{T}$ or $\tilde{T}$ (given in equation 27). $\tilde{T} = 0$ corresponds to the ejection time, and $\bar{T} = 0$ corresponds to the time when the first photons reach the observer. We show results for power-law and lognormal luminosities as a function of radii for three different values of the power-law index a and the standard deviation $\sigma_{\ln R}$, respectively.

4.3 Band spectrum emission for different dependences of the luminosity on radius

Using equation (15), we calculate the resulting light curve for a Band spectrum emission function with a low-energy photon index $\alpha_B = -1$ and a high-energy photon index $\beta_B = -2.3$, typical values obtained from fitting of GRB data. For the radial dependence of the emissivity, we use some specific functions for $f(R/R_0)$. For clarity, in all cases we take $\Gamma' = 3$, $m = 0$, $k = 0$. We plot two typical cases in Fig. 2: a power law in radius (equation 17) with $R_f = 2R_0$ and a Gaussian in $\ln(R)$:

$$f(R/R_0) = \frac{R_0/R}{\sqrt{2\pi}\,\sigma_{\ln R}} \exp\left(-\frac{[\ln(R/R_{0,\rm eff})]^2}{2{\sigma_{\ln R}}^2}\right), \tag{25}$$

where $R_{0,\rm eff} \equiv \exp({\sigma_{\ln R}}^2)R_0$ is a slightly different effective radius chosen such that $f(R/R_0)$ would peak at $R = R_0$. Note that $\sigma_{\ln R}$ can be related to the typical width in R through: $\Delta R \approx \sinh(\sigma_{\ln R})R_0$ (which for $\sigma_{\ln R} \ll 1$ yields $\Delta R \approx \sigma_{\ln R} R_0$). We plot the results at the frequency ν_p. The flux is given in units of the 'typical' peak flux,

$$F_0 \equiv \frac{2\Gamma_0 \Gamma'^{1-2k} L''_{\nu''_0}}{4\pi D^2}, \tag{26}$$

and the time in units of the typical time T_0, either starting at the observed ejection time $T_{\rm ej}$ (denoted as $\tilde{T}$) or starting at $T_{\rm ej} + T_0$, the time when the first photons reach the observer (this is defined as $\bar{T}$),

$$\tilde{T} \equiv \frac{T - T_{\rm ej}}{T_0}, \qquad \bar{T} \equiv \frac{T - T_0 - T_{\rm ej}}{T_0} = \tilde{T} - 1. \tag{27}$$

For a power-law emissivity, $f(R/R_0) \propto R^a$, the pulse shape becomes less symmetric and peaks at earlier times as a decreases. For a Gaussian $f(R/R_0)$, on the other hand, the peak occurs later for smaller typical widths (ΔR) but becomes more symmetric. The power-law and Gaussian cases approach the case of a delta function in radius and reproduces the result from Section 4.2 in the limits $a \to -\infty$ and $\Delta R \to 0$, respectively. We note also that in the Gaussian case the typical width of the pulse is $\sim \max(T_0/\Gamma', T_0 \Delta R/R_0)$ in accordance with equations (21) and (19).

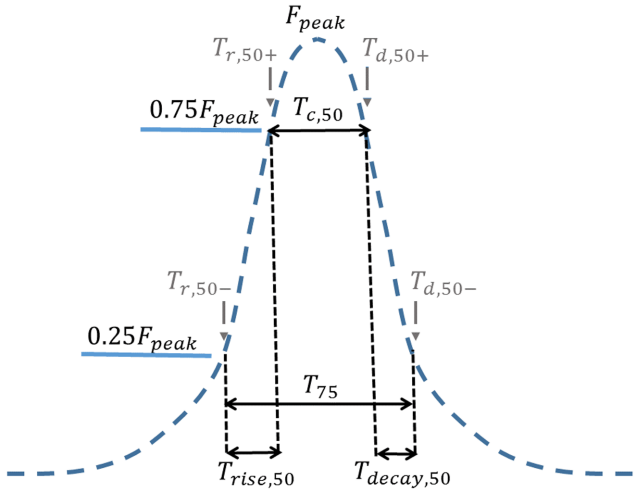

Figure 3. Schematic figure of the rise, decay and 'central' times defined in the text for $X = 50$. $T_{{\rm rise},X}$ ($T_{{\rm decay},X}$) is the time it takes the flux to rise (decay) from X_- per cent (X_+ per cent) to X_+ per cent (X_- per cent) of the peak value (where $X_\pm = (100 \pm X)/2$). $T_{c,X}$ is the time the flux stays above X_+ per cent of its peak value.

4.4 Exploring the single-pulse parameter space

Here, we explore the dependence of the single-pulse light curve on the various model parameters. We define $T_{r,Y}$ ($T_{d,Y}$) as the first time when the flux first (last) reaches Y per cent of its peak value. The rise (decay) time, is then defined by $T_{{\rm rise},X} \equiv T_{r,X_+} - T_{r,X_-}$ ($T_{{\rm decay},X} = T_{d,X_-} - T_{d,X_+}$) where $X_\pm = (100 \pm X)/2$. In addition, we define the 'central' time, $T_{c,X} \equiv T_{d,X_+} - T_{r,X_+}$ (see Fig. 3). Notice that if there is a significant 'plateau' stage, then it is possible that $T_{\rm rise}$, $T_{\rm decay} \ll T_c$. If the rise and decay of a pulse are monotonic, then $T_{100-X_-} \equiv T_{{\rm rise},X} + T_{c,X} + T_{{\rm decay},X} = T_{d,X_-} - T_{r,X_-}$ is the time spent at a flux above X_- per cent of the peak flux (analogous to the definition of GRB durations but with flux instead of fluence).

First, let us consider the more familiar case of non-boosted emission in the jet's bulk frame. If $\Delta R \lesssim R_0$ then the flux peaks

at approximately: $T = T_{\rm ej} + T_{\rm f}$, where $T_{\rm f} = (R_{\rm f}/R_0)^{m+1}T_0$, or $\bar{\rm T}_f = (R_{\rm f}/R_0)^{m+1} - 1 = [1 + (\Delta R/R_0)]^{m+1} - 1$. The rise time is then given by

$$\frac{T_{\rm rise}}{T_0} = \bar{T}_{\rm f} = \left(\frac{R_{\rm f}}{R_0}\right)^{m+1} - 1 = \left[1 + \frac{\Delta R}{R_0}\right]^{m+1} - 1 \xrightarrow[[\Delta R \ll R_0]]{} (m+1)\frac{\Delta R}{R_0}, \quad (28)$$

and the decay time $T_{\rm decay} \approx T_\theta(R_{\rm f})$ is given by

$$\frac{T_{\rm decay}}{T_0} = (m+1)\left(\frac{R_{\rm f}}{R_0}\right)^{m+1} = (m+1)\left[1 + \frac{\Delta R}{R_0}\right]^{m+1} \xrightarrow[[\Delta R \ll R_0]]{} (m+1)\left[1 + (m+1)\frac{\Delta R}{R_0}\right], \quad (29)$$

leading to a total pulse width $\Delta T = T_{\rm rise} + T_{\rm decay}$ of

$$\frac{\Delta T}{T_0} = (m+2)\left(\frac{R_{\rm f}}{R_0}\right)^{m+1} - 1 = (m+2)\left[1 + \frac{\Delta R}{R_0}\right]^{m+1} - 1 \xrightarrow[[\Delta R \ll R_0]]{} (m+1)\left[1 + (m+2)\frac{\Delta R}{R_0}\right], \quad (30)$$

which for $m = 0$ leads to $\Delta T/T_0 \sim R_{\rm f}/R_0$. For $\Delta R \gg R_0$, both the rise time and the decay time may be altered due to the emissivity function (see Table 1 for details), which (for the case of power-law luminosity as a function of radius and frequency) dominates the emission so long as $0.5 \lesssim \bar{T} < \bar{T}_{\rm f}$. The relevant parameter in this case is the power-law index q in the expression for $F_\nu(T) \propto T^q$. Using equation (19), we define

$$q = \frac{2a - m(1+\alpha)}{2(m+1)}. \quad (31)$$

Specifically for $q = 0$, the flux at this interval reaches an approximate plateau. This is an illustration of a situation in which $T_{\rm c} \gg T_{\rm rise}$. We define a quantitative measure of pulse asymmetry as $\Lambda \equiv T_{\rm rise}/T_{\rm decay}$. Pulses are asymmetric if $\Lambda \gg 1$ or $\Lambda \ll 1$. In fact, even for $\Lambda = 1$, the shape of the light curve could still be different between the rise and decay parts. For the non-boosted emission, we find that unless the emissivity is increasing with radius, then $\Lambda \ll 1$ (estimates for individual cases are listed in Table 1) implying shorter rise than decay time and a large degree of asymmetry regardless of the relation between ΔR and R_0. In fact, it is hard to produce very symmetric pulses ($\Lambda \approx 1$) for the case of such non-boosted emission, since the mechanisms controlling the rise and decay times are different. We now compare these results to the anisotropic case.

In Fig. 4, we plot the dependence of the pulse shape on the nature of the emission: continuous, single blob and non-boosted emission, for a constant comoving luminosity with $\Delta R/R_0 = 0.1$. For $\Delta R < R_0$, the flux peaks earlier for non-boosted emission than for the cases with anisotropy. The light curve is sharper and less symmetric for the non-boosted emission so long as $\Delta R < R_0/\Gamma'$. This arises since for $\Delta R < R_0/\Gamma'$ in the non-boosted case the pulse rise time is determined by ΔR ($\bar{T}_{\rm rise} \sim \Delta R/R_0$) while its decay time is $T_{\rm decay} \sim T_0$, whereas in the anisotropic case the pulse is rather symmetric ($\Lambda \approx 1$), since $\bar{T}_{\rm rise} \sim \bar{T}_{\rm decay} \sim 1/\Gamma'$ (and its width reflects that for the emission from a single radius). To easily understand the latter expression, consider that the emission from each radius is dominated by two regions of angular size $\sim 1/(\Gamma'\Gamma)$ around the two points of the intersection of the x'-axis (where $\boldsymbol{\beta'} = \pm\beta'\hat{x'}$) and the circle $\theta = 1/\Gamma$, or $\xi = (\Gamma\theta)^2 = 1$ (see Fig. 5 and Section B). This dominant contribution arrives over a time $\sim T_0/\Gamma'$, which is thus the 'smearing time-scale' compared to the very large Γ' limit. In the right-hand panel of Fig. 4, we plot also the dependence of the light curve on m for the anisotropic case. As shown in Section 4.2 (and can be seen for the non-boosted case from equation 28), in terms of the normalized time $\bar{T}$ the peak occurs at $\bar{T} \approx m + 1$, which is when the beaming cone points towards the observer, after accounting for the aberration of light for the jet's frame to the observer's frame. This behaviour, of the peak occurring at a later time for a larger m, can indeed be seen in the right-hand panel of Fig. 4.

In Fig. 6, we plot the dependence of the pulse shape on the values of Γ'. Once $\Gamma' \gg 1$ and $1/\Gamma' \ll \Delta R/R_0$, the pulse's shape does not depend strongly on Γ', and is set instead by $f(R/R_0)$. This is because in this case, the typical times related to the emissivity function are larger than the pulse width from a single radius, $\Delta T \sim T_0/\Gamma'$. The top-right panel of Fig. 6 shows light curves for $\Delta R/R_0 = 1$ and a lognormal radial dependence of the comoving emissivity. It demonstrates that for $\Delta R \sim R_0$ with a smooth turn-on and turn-off of the emissivity, as might typically be expected, the pulse-shape for anisotropic emission is not very different from that of non-boosted emission, showing a similarly noticeable degree of asymmetry ($\Lambda_{50} \approx 0.107$, $\Lambda_{90} \approx 0.096$ for the non-boosted case as opposed to $\Lambda_{50} \approx 0.118$, $\Lambda_{90} \approx 0.173$ for the anisotropic case). The asymmetry becomes larger for $\Delta R \gg R_0$ (and remains independent of Γ'). This is because the rise time is dominated by the radial time-scale at the point where the emissivity function is within 1σ of the peak, i.e. $R_i \approx R_0^2/\Delta R \Longrightarrow T_{\rm rise} \sim (R_0/\Delta R)^{m+1}$, whereas the decay time is dominated by the radial time-scale where the emissivity function is 1σ above the peak: $R_{\rm f} \approx \Delta R \Longrightarrow T_{\rm decay} \sim (\Delta R/R_0)^{m+1}$. This leads to $\Lambda \sim (R_0/\Delta R)^{2(m+1)}$ (in fact, there is a numerical pre-factor here of the order of 0.1 arising from the smooth shape of the lognormal function's decline, see Table 1). Slightly asymmetric pulses are in broad agreement with the typical observed pulse shape. On the other hand, symmetric pulses are also sometimes observed, and are hard to produce with non-boosted emission, but rather easy to produce for anisotropic emission. A summary of the typical times for the various cases is given in Table 1. The expected asymmetry measures in our model can be seen explicitly in Fig. 7 where we plot the value of Λ for different values of Γ', $\Delta R/R_0$ and for different assumptions on the emissivity as a function of radius.

4.5 Correlation between Γ' and $\gamma'_{\rm e}$

Here, we explore the implications of a possible correlation between Γ' and the random Lorentz factor of the electrons in the bulk frame $\gamma'_{\rm e}$ such that $\Gamma' = K\gamma'^{\eta}_{\rm e}$. Correlations of this kind may result in case the reconnection layer is continuously fed by incoming particles (i.e. $k = 1$) and a quasi-steady state is achieved between incoming and outgoing particles. This behaviour has previously been found in PIC simulations (e.g. Cerutti et al. 2012, 2013). There is a physical motivation for this since the electrons that are accelerated to higher energies are preferentially those that spend a longer time being accelerated in the reconnection layer, and thus their velocities tend to be more tightly collimated, down to a scatter of $\Delta\theta \sim 1/\gamma'_{\rm e}$. This can be understood in the following way. The electric field in the reconnection layers is perpendicular to both the original magnetic field's direction and to the incoming particles' velocities. Electrons are only accelerated as long as they have not deflected significantly from the X-point and move along the electric field E. If this acceleration is over a distance $l_\parallel$, then they acquire an energy of $\gamma'_{\rm e} m_{\rm e} c^2 \approx eEl_\parallel \approx \beta_{\rm in} eB_0 l_\parallel$, where B_0 is the magnetic field strength in the bulk, before the reconnection layer. On the other hand, they

MNRAS 459, 3635–3658 (2016)

Table 1. Properties of observed light curves for single pulses with different assumptions on the Lorentz factor of the emitters (Γ') and q the power-law index of T in the expression for $F_\nu(T)$.

Case	Width	Γ'	$f(R)$	$\bar{T}_{\rm rise,X}$	$\bar{T}_{\rm decay,X}$	Λ	$\bar{T}_{\rm c,X}$	Description
1	$\Delta R \ll R_0$	$\Gamma'=1$	Any	$\bar{T}_{\rm f}\approx(m+1)\frac{\Delta R}{R_0}$	$\tilde{T}_\theta(R_{\rm f})$	$\frac{\Delta R}{R_0}\ll 1$	$\bar{T}_{\rm rise}\ll\bar{T}_{\rm c}\ll\bar{T}_{\rm decay}$	Asymmetric, no plateau
2	$\Delta R \ll R_0$	$\frac{\Delta R}{R_0}<\frac{1}{\Gamma'}<1$	Any	$\frac{1}{\Gamma'}$	$\frac{1}{\Gamma'}$	1	$\bar{T}_{\rm c}\lesssim\bar{T}_{\rm rise}+\bar{T}_{\rm decay}$	Symmetric, no plateau
3	$\Delta R \ll R_0$	$\frac{1}{\Gamma'}<\frac{\Delta R}{R_0}<1$	PL; any q	$\frac{1}{\Gamma'}$	$\frac{1}{\Gamma'}$	1	$\bar{T}_{\rm c}\approx\frac{\Delta R}{R_0}\gg\bar{T}_{\rm rise}\sim\bar{T}_{\rm decay}$	Symmetric, short plateau
4	$\Delta R \ll R_0$	$\frac{1}{\Gamma'}<\frac{\Delta R}{R_0}<1$	lognormal	$\bar{T}_{\rm f}\approx(m+1)\frac{\Delta R}{R_0}$	$\bar{T}_f\approx(m+1)\frac{\Delta R}{R_0}$	1	$\bar{T}_{\rm c}\lesssim\bar{T}_{\rm rise}+\bar{T}_{\rm decay}$	Symmetric, no plateau
5	$\Delta R \gg R_0$	$\Gamma'=1$	PL; $q<0$[a]	$\tilde{T}_\theta(R_0)=1$	$\bar{T}_{\rm f}$	$\left(\frac{R_0}{R_{\rm f}}\right)^{m+1}$	$\bar{T}_{\rm rise}\ll\bar{T}_{\rm c}\approx\bar{T}_{\rm decay}\approx\left(\frac{\Delta R}{R_0}\right)^{m+1}$	Asymmetric, no plateau
6	$\Delta R \gg R_0$	$\Gamma'=1$	PL; $q=0$	$\tilde{T}_\theta(R_0)=1$	$\bar{T}_\theta(R_{\rm f})$	$\frac{(R_0/R_{\rm f})^{m+1}}{m+1}\ll 1$	$\bar{T}_{\rm rise}\ll\bar{T}_{\rm c}\approx\bar{T}_{\rm decay}\approx\left(\frac{\Delta R}{R_0}\right)^{m+1}$	Asymmetric, with plateau
7	$\Delta R \gg R_0$	$\Gamma'=1$	PL; $q>0$[b]	$\bar{T}_{\rm f}$	$\bar{T}_\theta(R_{\rm f})$	$\frac{1}{m+1}$	$\bar{T}_{\rm c}\lesssim\bar{T}_{\rm rise}+\bar{T}_{\rm decay}$	Asymmetric, no plateau
8	$\Delta R \gg R_0$	$\Gamma'>1$	PL; $q<0$[a]	$\frac{1}{\Gamma'}$	$\bar{T}_{\rm f}$	$\frac{1}{\Gamma'}\left(\frac{R_0}{R_{\rm f}}\right)^{m+1}\ll 1$	$\bar{T}_{\rm c}\ll\bar{T}_{\rm rise}+\bar{T}_{\rm decay}$	Asymmetric, no plateau
9	$\Delta R \gg R_0$	$\Gamma'>1$	PL; $q=0$	$\frac{1}{\Gamma'}$	$\frac{\tilde{T}_\theta(R_{\rm f})}{\Gamma'}$	$\frac{(R_0/R_{\rm f})^{m+1}}{m+1}\ll 1$	$\bar{T}_{\rm c}\approx\left(\frac{\Delta R}{R_0}\right)^{m+1}\gg\bar{T}_{\rm decay}\gg\bar{T}_{\rm decay}$	Asymmetric, with plateau
10	$\Delta R \gg R_0$	$\Gamma'>1$	PL; $q>0$[b]	$\bar{T}_{\rm f}$	$\frac{\tilde{T}_\theta(R_{\rm f})}{\Gamma'}$	$\frac{\Gamma'}{m+1}$	$\bar{T}_{\rm c}\approx\bar{T}_{\rm rise}\gg\bar{T}_{\rm decay}$	Asymmetric, no plateau
11	$\Delta R \gg R_0$	any Γ'	lognormal	$\bar{T}_i\approx\left(\frac{R_0}{\Delta R}\right)^{m+1}$	[c]$10\bar{T}_{\rm f}\approx 10\left(\frac{\Delta R}{R_0}\right)^{m+1}$	$0.1\left(\frac{R_0}{\Delta R}\right)^{2(m+1)}\ll 1$	$\bar{T}_{\rm rise}\ll\bar{T}_{\rm c}\ll\bar{T}_{\rm decay}$	Asymmetric, no plateau

Notes. [a]Assuming that $(100-X)/2<f(\bar{T}_{\rm f})/f(\bar{T}_0)<(100+X)/2$. In case $f(\bar{T}_{\rm f})/f(\bar{T}_0)>(100+X)/2$ the situation reduces back to that obtained at $q=0$, while if $f(\bar{T}_{\rm f})/f(\bar{T}_0)<(100-X)/2$ then the decline time stops increasing with ΔR and instead remains fixed on the value $\sim\bar{T}_{\rm f*}$ obtained for $f(\bar{T}_{\rm f})/f(\bar{T}_0)=(100-X)/2$ with $\Lambda\sim(\Gamma'\bar{T}_{\rm f*})^{-1}\propto 1/\Gamma'$.
[b]Assuming that $f(\bar{T}_{\rm f})/f(\bar{T}_0)>\frac{100+X}{100-X}$. In case the increase with radius is shallower, the situation reduces back to that obtained at $q=0$.
[c]As it turns out, due to the smooth shape of the lognormal function, the decay time is approximately 10 times larger than $\bar{T}_{\rm f}$.

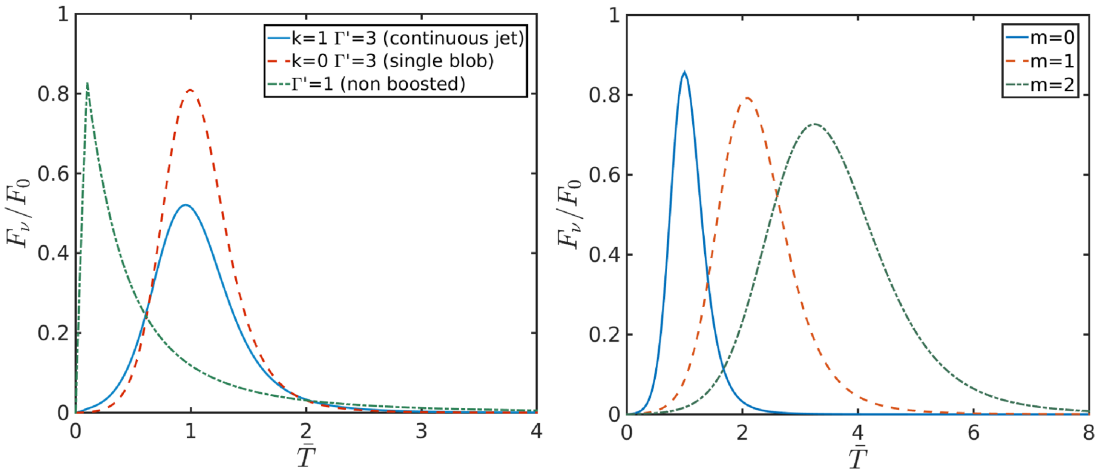

Figure 4. Left: single-pulse light curves for different assumptions on the emission (continuous and steady in the jet's bulk frame versus single blob versus non-boosted emission). All cases are plotted with a typical Band function spectral emissivity, a constant dependence of luminosity on the radius with $R_f = 1.1R_0$ as well as $m = 0$. The flux is given in units of the 'typical' peak flux F_0 as a function of the normalized time $\bar{T}$. Right: light curves with $k = 0$, $\Gamma' = 3$, a constant dependence of luminosity on the radius with $R_f = 1.1R_0$ and different values of m.

exit the acceleration site after traversing a distance $l_\perp$ in the perpendicular direction, at which point their angle relative to the electric field direction is

$$\theta \sim \frac{l_\perp}{l_\parallel} \sim \frac{\beta_{in} l_\perp e B_0}{\gamma_e' m_e c^2} \approx \frac{\beta_{in} l_\perp}{R_L(B_0)} \propto \frac{1}{\gamma_e'} . \quad (32)$$

It follows that Γ' may be up to linear in γ_e' (see equation C5 in Section C) and that one might naively expect $0 \leq \eta \leq 1$.

In the presence of such a correlation, electrons of different typical energies may dominate the emission at different observed frequency bands. This leads to a qualitatively different physical scenario than that presented elsewhere in the text. The main difference from the case with no $\Gamma'-\gamma_e'$ correlation has to do with determining the frame in which the electric field vanishes. In case a correlation between Γ' and γ_e' exists, electrons of different energies are experiencing different fields and, contrary to the case with no correlation, there is no single primed frame where the electric field vanishes and where electrons can gyrate freely around the magnetic field without their velocities getting isotropized in the jet's frame. Here, the role of the vanishing electric field frame is played by the jet's frame.[1] As a result, in order for the electrons' emission to remain beamed, they must radiate a significant fraction of their energy before their velocities get isotropized in the jet (rather than the plasmoids') frame (i.e. within less than a single Larmour gyration). Therefore, such a correlation can be expected to manifest itself only at very high frequencies – at a band near the classical 'maximal synchrotron energy'. We stress that the results obtained under these assumptions are therefore likely not to be relevant for understanding the observed properties of sub-MeV pulses. However, they may still have interesting observable implications for the high-energy emission.

Notice that the emitters with different γ_e' have different Γ' corresponding to different CM frames. Moreover, the average electrons' Lorentz factor in the emitters' frame, γ_e'', is related to γ_e' through

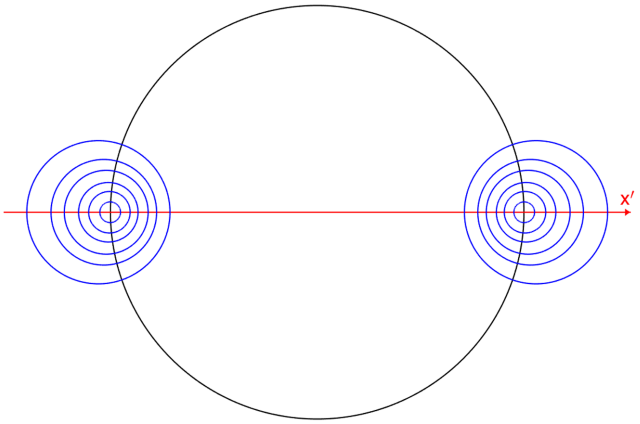

Figure 5. The emission region – the blue contours show the area within the emitting spherical shell that is within the beaming cone of the emitting material in the jet's bulk frame, i.e. where $\hat{n}'$ is within an angle of $1/\Gamma'$ from the direction of its velocity $\hat{\beta}' = \pm\hat{x}'$, for $\Gamma' = 3, 4, 5, 7, 10, 20$. The big black circle indicates an angle of $\theta = 1/\Gamma$ around the line of sight to the central source, while the red arrow shows the x'-axis.

Γ': $\gamma_e' \approx \Gamma'\gamma_e''$ (see Section C for a derivation). It follows that:

$$\gamma_e' = \left(\frac{\Gamma'}{K}\right)^{1/\eta} = \Gamma'\gamma_e'' \quad \Longrightarrow \quad \Gamma' = K^{1/1-\eta}\gamma_e''^{\eta/1-\eta} . \quad (33)$$

In addition, if we assume that the emission is dominated by synchrotron radiation (as expected in a magnetically dominated emission region), then $\nu_{syn}' = \frac{eB'}{2\pi m_e c}\gamma_e'^2$, where B' is the magnetic field strength in the jet's bulk frame (which is expected to be roughly constant for particles of different energy, as they are all assumed to radiate in a similar location). It can be related to the magnetic field in the emitter's frame through[2] $B'' \approx B'\Gamma'$. It is useful to relate the

[1] In the acceleration region (or X point), where $E^2 > B^2$, there is no frame where the electric field vanishes. However, the radiation occurs mostly outside of this region, in the jet's bulk frame.

[2] This is different from the usual relation that is derived under the assumption that there is a single primed frame where the electric field vanishes.

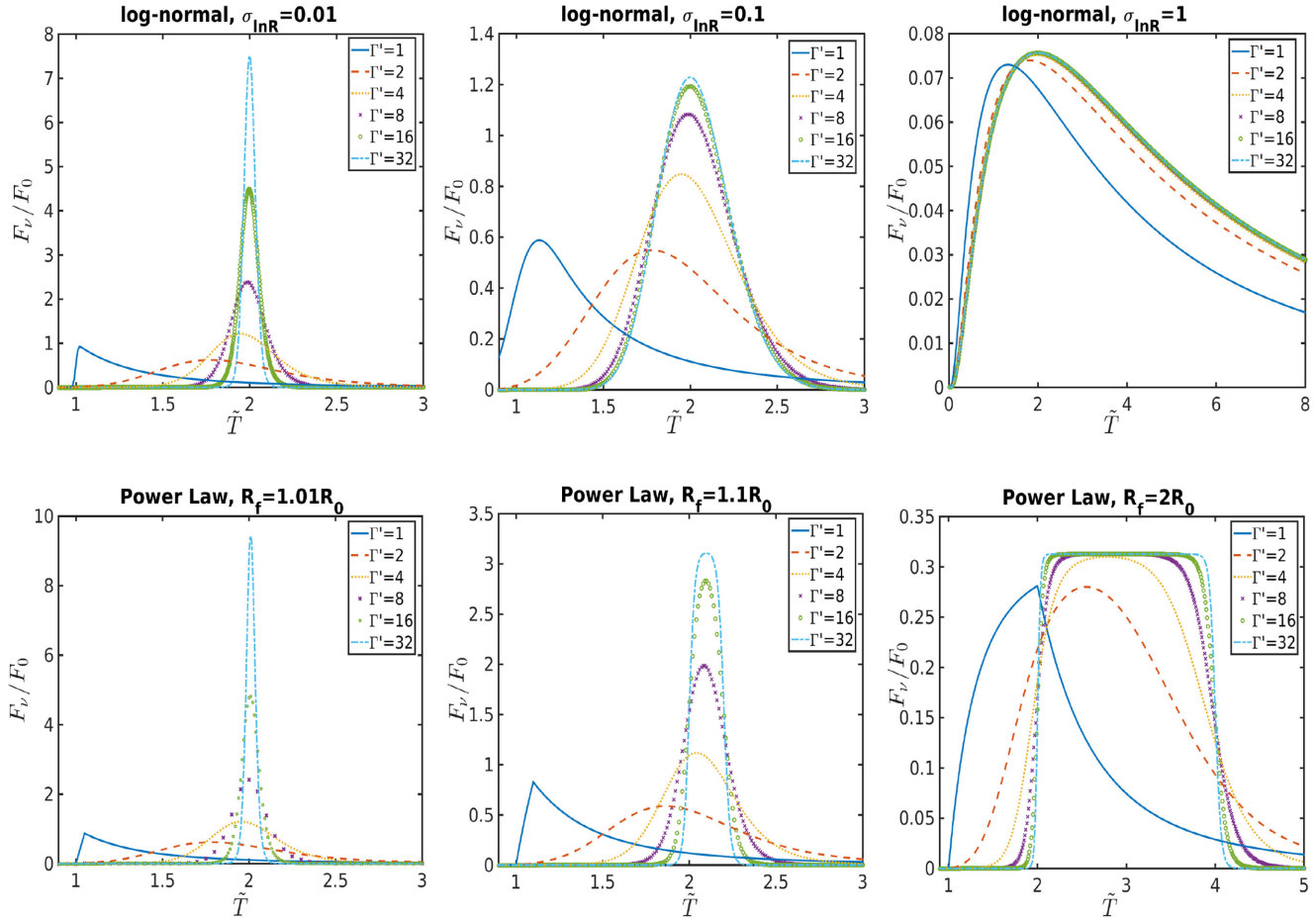

Figure 6. Light curves of a pulse assuming different values of the emitter's Lorentz factor Γ' ($\log_2(\Gamma') = 0, 1, 2, 3, 4, 5$) with $m = 0$ and $k = 0$. The flux is given in units of F_0 as a function of the normalized time $\tilde{T}$. Top panels: results for a lognormal dependence of luminosity on radius with different typical widths ($\sigma_{\rm lnR} = 0.01, 0.1, 1$ from left to right). Bottom panels: results for a constant dependence of luminosity on radius with different typical widths ($\Delta R/R_0 = (R_{\rm f} - R_0)/R_0 = 0.01, 0.1, 1$ from left to right).

observed frequency to Γ':

$$\nu = \nu_{\rm syn}(\gamma_{\rm e}') \approx \Gamma \nu_{\rm syn}'(\gamma_{\rm e}') = \frac{\Gamma e B'}{2\pi m_{\rm e} c}\left(\frac{\Gamma'}{K}\right)^{2/\eta}. \quad (34)$$

Since the peak spectral emissivity is determined in the jet's bulk frame. The spectrum in this frame is given by the regular synchrotron formulas. As detailed above, a correlation between $\gamma_{\rm e}'$ and Γ' implies that the electric field vanishes only in the jet's (rather than the plasmoids') frame and as a result we should consider electrons in the 'fast cooling' regime (i.e. that cool significantly in less than a dynamical time), and so the particles' spectrum is

$$\frac{{\rm d}N_{\rm e}}{{\rm d}\gamma_{\rm e}'} = A\gamma_{\rm e}'^{-p-1} \iff \frac{{\rm d}N_{\rm e}}{{\rm d}\ln\gamma_{\rm e}'} = A\gamma_{\rm e}'^{-p}. \quad (35)$$

The resulting spectrum is therefore: $P_\nu \propto \nu^{-p/2}$ as for the case of synchrotron without boosted emission in the jet's bulk frame.

Although the spectrum does not change for $\Gamma' \gg 1$, there will be an angle dependent cut-off to the spectrum in this case. Notice that electrons with different Lorentz factors $\gamma_{\rm e}'$ are emitted by emitters with different Γ'. Emission from an emitter moving at Γ' can be seen up to an angle $\theta_{\rm obs}' \approx 1/\Gamma'(\gamma_{\rm e}')$ where $\cos\theta_{\rm obs}' = \hat{n}' \cdot \hat{\beta}'$, this implies a cut-off of the observed spectrum that is determined by the observation angle:

$$\nu_{\rm max}\left(\theta_{\rm obs}'\right) = \nu_{\rm obs}\left(\Gamma' = 1/\theta_{\rm obs}'\right) = \frac{\Gamma e B'}{2\pi m_{\rm e} c}\left(K\theta_{\rm obs}'\right)^{-2/\eta}. \quad (36)$$

As mentioned above, in order to maintain the anisotropy, electrons are doing less than one gyration around the magnetic field. Therefore, this effect will take place at frequencies above the 'regular' maximal synchrotron frequency $\nu_{\rm syn,\,max}$.

Another effect introduced by a correlation of the type $\Gamma' \propto \gamma_{\rm e}'^{\eta}$ relates to the typical width of the pulses. So long as the latter are determined by Γ' (see Section 4.4 for details), the typical width will be different at different frequencies (which are dominated by emission from electrons at different energies). As seen by equation (34), this will lead to $\Delta T \propto \nu^{-\eta/2}$. We return to this point in Section 5.3.

As is the usual case for synchrotron, we can safely assume that each frequency is dominated by electrons of a single energy.[3] As mentioned above, the only frame with a purely magnetic field in case of a $\Gamma' - \gamma_{\rm e}'$ correlation, is the jet's frame. We therefore start with the peak spectral emissivity of individual electrons in the jet's frame ($P_{\nu',{\rm e,max}}' \approx \sigma_T m_{\rm e} c^2 B'/(3e) \propto B'$) and use the regular

[3] This is true so long as the spectrum obtained in this way is softer than the synchrotron spectrum for single electrons: $F_\nu \propto \nu^{1/3}$.

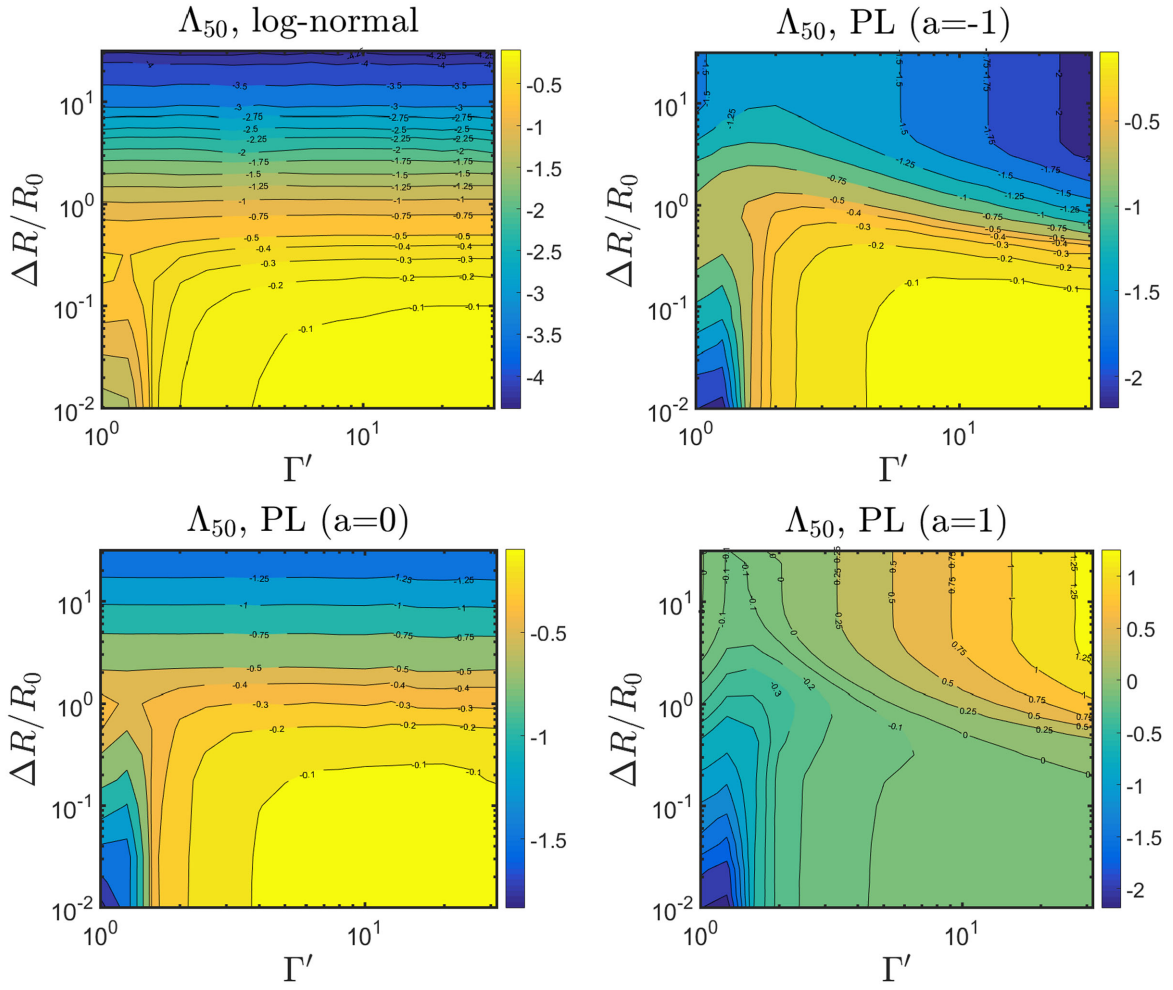

Figure 7. The asymmetry ratio: $\Lambda_{50} \equiv T_{\rm rise,50}/T_{\rm decay,50}$ as a function of Γ' and $\Delta R/R_0$. All plots are for $k = 0$, $m = 0$ and a power-law spectrum with $\alpha = 1$. Top-left: results for lognormal emissivity as a function of radius. Top-right: results for PL emissivity as a function of radius with $a = -1$ (corresponding to $q = -1$). Bottom-left: results for PL emissivity as a function of radius with $a = 0$ (corresponding to $q = 0$). Bottom-right: results for PL emissivity as a function of radius with $a = 1$ (corresponding to $q = 1$).

Lorentz transformation (as in equation 8, but with the direction of the transformation reversed) to obtain the (isotropic) luminosity in the emitters' frame:

$$L''_{\nu''} = \int {\rm d}\Omega' \int {\rm d}\gamma'_{\rm e}\delta(\gamma'_{\rm e} - \gamma'_{\rm e,syn}) L'_{\nu'}(\gamma'_{\rm e,syn}) \mathcal{D}'(\gamma'_{\rm e})^{k-3}\Gamma'(\gamma'_{\rm e})^{k}$$
$$\approx \int {\rm d}\Omega' \frac{{\rm d}N_{\rm e}}{{\rm d}\ln\gamma'_{\rm e}}(\gamma'_{\rm e,syn})\, L'_{\nu',{\rm e,max}}\, \mathcal{D}'(\gamma'_{\rm e,syn})^{k-3}\Gamma'(\gamma'_{\rm e,syn})^{k}$$
$$\times \sim A\gamma'^{-p}_{\rm e,syn}\frac{P'_{\nu',{\rm e,max}}}{\Gamma'(\gamma'_{\rm e,syn})}, \qquad (37)$$

where $\gamma'_{\rm e,syn}$ is the Lorentz factor (in the jet's frame) of electrons for which the synchrotron frequency is the observed frequency ν:

$$\gamma'_{\rm e,syn} = \left(\frac{\nu 2\pi m_{\rm e} c K}{\mathcal{D}(y)\mathcal{D}'(y,\phi) e B'}\right)^{1/2-\eta}. \qquad (38)$$

Note that in equation (37), we have expressed the spectral luminosity in the jet's frame ($L'_{\nu'}$) in terms of the electrons' energy distribution (${\rm d}N_{\rm e}/{\rm d}\gamma'_{\rm e}$) and the peak luminosity of individual electrons ($L'_{\nu',{\rm e,max}}$), where $L'_{\nu'}(\gamma'_{\rm e,syn})/L'_{\nu',{\rm e,max}} \approx \frac{{\rm d}N_{\rm e}}{{\rm d}\ln\gamma'_{\rm e}}(\gamma'_{\rm e,syn}) \approx N_{\rm e}(\gamma'_{\rm e,syn})$ is the number of electrons whose synchrotron frequency is close to the observed frequency, so that each of these electrons radiates at that frequency near its peak spectral power $P'_{\nu',{\rm e,max}}$ or its peak isotropic equivalent spectral luminosity $L'_{\nu',{\rm e,max}}$. The latter are related through $L'_{\nu',{\rm e,max}} \sim \Gamma'^2 P'_{\nu',{\rm e,max}}$, since $P'_{\nu'} = {\rm d}E'/{\rm d}\nu'{\rm d}t'$ and $L'_{\nu'} = 4\pi({\rm d}E'/{\rm d}\nu'{\rm d}t'{\rm d}\Omega') = 4\pi({\rm d}P'_{\nu'}/{\rm d}\Omega') \sim (4\pi/\Delta\Omega')P'_{\nu'}$ and in our case $4\pi/\Delta\Omega' \approx 4\Gamma'^2 \sim \Gamma'^2$ as because of relativistic beaming, in the jet's frame, the contribution of the luminosity is significant only within a cone of opening angle $\sim 1/\Gamma'$ in which $\mathcal{D}' \sim \Gamma'$. The basic result of equation (37) is that $L''_{\nu''} \sim N_{\rm e}(\gamma'_{\rm e,syn})P'_{\nu',{\rm e,max}}/\Gamma'(\gamma'_{\rm e,syn})$ or that in the emitters' frame the spectral power of a single electron whose synchrotron frequency is close to the observed one, satisfies $P''_{\nu',{\rm e,max}} \approx L''_{\nu''}/N_{\rm e}(\gamma'_{\rm e,syn}) \sim P'_{\nu',{\rm e,max}}/\Gamma'(\gamma'_{\rm e,syn})$, which is the usual familiar Lorentz transformation for the received emission in the jet's frame, which corresponds to a single propagating electron, e.g. that is part of a blob and so corresponds to $k = 0$. The correction for a steady state in the jet's frame, $k = 1$, is the extra power of $1 - \beta'(\gamma_{\rm e,syn})\sin\theta'\cos\phi$ (which is the ratio of the received and emitted times for a point source such as an individual electron) that appears in equation (39), which accounts for the fact that in this case there is no distinction between the emitted and received times, so that the radiation is not received over a shorter time than it is emitted, as is the case for a blob.

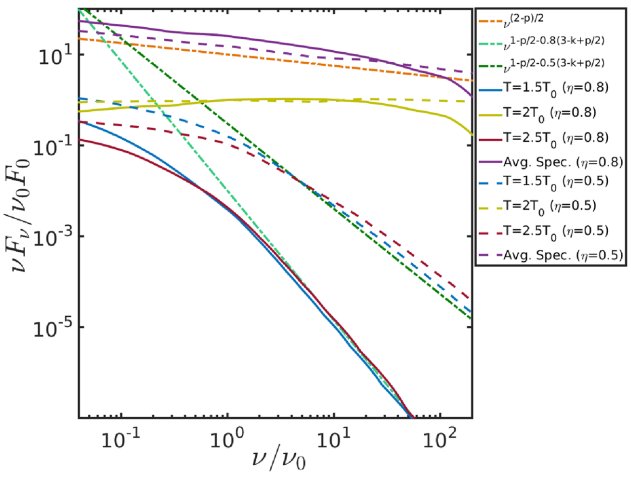

Figure 8. Spectra of a single pulse at different times: $T = [1.5, 2, 2.5]T_0$, alongside the time-averaged spectrum, assuming a correlation of the type $\Gamma' \propto \gamma_e'^{\eta}$. The electrons' energy distribution is assumed to be $\frac{dN_e}{d\gamma_e'} \propto \gamma_e'^{-1-p}$, with $p = 2.5$. We also assume $m = 0$, $k = 1$ and a lognormal emissivity with $\sigma_{\ln R} = 0.01$. The peak of the light curve is at $T = 2T_0$. The spectra is plotted for $\eta = 0.8$ (solid lines) and $\eta = 0.5$ (dashed lines). For comparison, we also plot the expected spectrum in this case, for non-boosted emission (and for the time-averaged spectrum): $\nu F_\nu \propto \nu^{2-p/2}$, and the asymptotic spectrum expected in this case for $\nu > \nu_{\max}$. The frequency is in units of ν_0, which is the typical frequency at which electrons with $\Gamma' = 100$ radiate (see equation 34), and below which the time-scale is dominated by the radial instead of the angular one. νF_ν is given in the units of $\nu_0 F_0$, where F_0 is the peak of the time-resolved flux at ν_0.

In order to obtain the observed flux, we plug equation (37) into equation (15) and integrate over γ_e':

$$F_\nu(T) = \frac{2\Gamma_0 A P'_{\nu',e,\max}}{(4\pi)^2 D^2}\left(\frac{T}{T_0}\right)^{-m/2(m+1)} \times \int_{y_{\min}}^{y_{\max}} dy \left(\frac{m+1}{m+y^{-m-1}}\right)^2 y^{-1-m/2} f\left[y\left(\frac{T}{T_0}\right)^{1/m+1}\right] \times \int_0^{2\pi} d\phi \frac{\gamma_{e,syn}^{-p}}{2K^4\gamma_{e,syn}^{4\eta}}(1-\beta'(\gamma_{e,syn})\sin\theta'\cos\phi)^{k-3} . \quad (39)$$

The resulting spectrum is shown in Fig. 8. The time integrated spectrum, as well as the spectrum close to the time of the peak flux approach $\nu F_\nu \propto \nu^{2-p/2}$ as expected for non-boosted emission. Results are plotted for $p = 2.5$ which is consistent with expectations from theory. Note that although for acceleration in reconnection sites a large range of p-values is found, depending on the exact setup and initial magnetization (Guo et al. 2014, 2015; Sironi & Spitkovsky 2014; Werner et al. 2016; Kagan et al. 2015) down to values of the order of $p \approx 1.5$, this of course cannot hold up to very large energies as they would require a divergence of the total energy, and is also inconsistent with both afterglow observations and observations of the high-energy spectral slope of the Band function. At either early or late times, and frequencies above $\nu_{\max}$, the flux will become steeper, due to the angle-dependent cut-off described in equation (36). For these, the emission is dominated by large angles from the line of sight, with $\theta'\Gamma'(\nu) > 1$, and one can relate the observed spectrum $F_\nu(\theta')$ to the one along the line of sight, $F_\nu(\theta' = 0) = F_\nu(0)$ (e.g. Granot et al. 2002; Granot, Ramirez-Ruiz & Perna 2005),

$$\frac{F_\nu(\theta)}{F_\nu(0)} = \left(\frac{\mathcal{D}'(\theta')}{\mathcal{D}'(0)}\right)^{3-k+p/2} \approx \left[1+(\Gamma'\theta')^2\right]^{k-3-p/2} \times \propto \gamma_e'^{2\eta(k-3-p/2)} \propto \nu^{-\eta(3-k+p/2)} ,$$
$$\implies \quad F_\nu(\theta) \propto F_\nu(0)\nu^{-\eta(3-k+p/2)} \propto \nu^{-p/2-\eta(3-k+p/2)} . \quad (40)$$

Fig. 8 clearly shows that at early and late times, the flux approaches this slope. The transition from the $\nu^{-p/2}$ slope to this steeper slope, is at $\nu_{\max}$.

4.6 Results for the entire light curve

Under the same assumptions as in Section 4.3, and for the same dependences of the luminosity on radius we calculate the resulting light curve. In principle, the distributions of luminosities, Lorentz factors and typical radii of emission, are model dependent, and are not uniquely determined by the fact that there is anisotropic emission in the jet's bulk frame. These can reflect the inner workings of the central engine (see Section 6 for more details). Since we do not want to invoke a specific central engine model, these distributions were chosen phenomenologically, motivated by typical light-curve observations. We assume that individual shells (leading to different pulses) are characterized by different typical duration T_0, different ejection times T_{ej}, different Γ' and different peak luminosities (i.e. different F_0). We assumed 10 spikes in the light curve, corresponding to 10 emitting shells. In order to calculate the corresponding light curve from 10 shells, we randomly draw the parameters of each shell out of the following probability distributions. We draw the values of T_0 for different shells from a lognormal distribution with a central value denoted as $\langle T_0\rangle$ and a typical width of 0.3 dex. The ejection times T_{ej} are randomly drawn from a uniform distribution in the range $0 \le T_{ej} \le 20\langle T_0\rangle$. We draw the values of Γ' for different shells from either a uniform distribution between 2 and 10 (or between 1 and 10). Finally, we draw the luminosities ($L''_{\nu_0''}$) from a lognormal distribution with a central value denoted as $\langle L''_{\nu_0''}\rangle$ and a typical width of 0.5 dex. The results are plotted in Fig. 9. For larger $\Delta R/R_0$ and for $a = 0$, the pulses tend to be wider (and the peak flux is weaker in order to conserve the total luminosity of the pulse). In this case, it is harder to resolve individual pulses and there is more overlapping of pulses. Generally, the resulting light curves can be quite complex and have a wide range of typical behaviours, as seen in observations. However, it is basically a reflection of the choice of distributions above and therefore a true comparison with observations will depend on the specific model assumed.

5 COMPARISON WITH OBSERVATIONS

5.1 Peak luminosity–variability correlation

Several studies have explored the possibility that the variability of GRB light curves is related to their peak luminosities (Stern, Poutanen & Svensson 1999; Fenimore & Ramirez-Ruiz 2000; Reichart et al. 2001). We use the definition for the variability presented in Kobayashi, Ryde & MacFadyen (2002), which is a simplified version of that in Reichart et al. (2001):

$$V = \frac{\sum(F_\nu(T) - \langle F_\nu(T)\rangle)^2}{\sum F_\nu(T)^2}, \quad (41)$$

where $\langle F_\nu(T)\rangle$ is the flux smoothed with a boxcar window with a time-scale equal to the smallest fraction of the burst time history

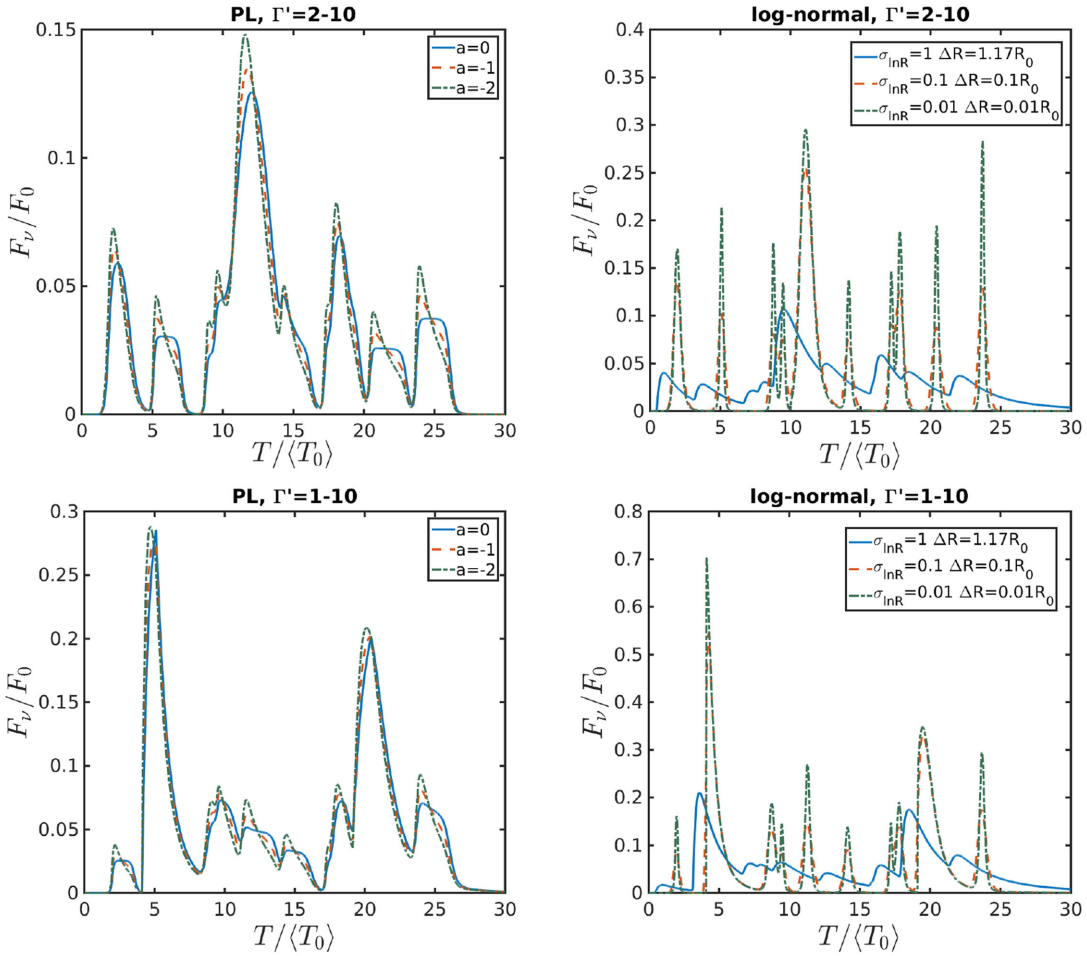

Figure 9. Light curves of 10 consecutive pulses with different $L(R)$ (but the same for different pulses within a light curve). We assume a Band function spectrum and $m = 0$, $k = 0$. The flux is in units of the 'typical' peak flux $F_0(\Gamma' = 1)$ as a function of the average normalized time $T/\langle T_0\rangle$. T_0, $L''_{\nu''_0}$ for different shells are lognormally distributed with widths of 0.3, 0.5 dex correspondingly. The ejection times are uniformly distributed in the range $0 \leq T_{\rm ej} \leq 20\langle T_0\rangle$. Finally, Γ' is uniformly distributed in the range 2–10 (1–10) in the top (bottom) panels. Left: power law $L(R)$ with different power-law slopes a and $R_{\rm f} = 2R_0$. Right: lognormal $L(R)$ with different standard deviations $\sigma_{\ln R}$. All parameters (except for Γ') are held constant for different light curves within any panel. The values of Γ' in the top (bottom) panel, from left to right, are: 3.4, 9, 9.6, 2.6, 8, 7.6, 9.8, 5.5, 9.7, 6.4 (8, 1.1, 4.6, 7.4, 9.3, 5.5, 1.3, 4.6, 6.7, 8.1).

that contains a fraction 0.45 of the total flux. Reichart et al. (2001) have found that the peak luminosities L are correlated with the variability measures: $L_{\rm max} \propto V^{3.3^{+1.1}_{-0.9}}$. It should however be noted that other studies (Guidorzi 2005; Guidorzi et al. 2005) have claimed a correlation with a much shallower slope, of the order of $1.30^{+0.84}_{-0.44}$ and 0.85 ± 0.02, respectively. The difference between the results has been attributed to their respective treatment of sample variance (Guidorzi et al. 2006). These authors use a Monte Carlo method to show that when the sample variance is of order the total variance the latter methods become more reliable estimators of the slope in the $L_{\rm max}$–V correlation.

A correlation between peak luminosity and variability may also be expected in our model, since the peak luminosity increases with Γ' and the width of pulses decreases with Γ' so long as $\Delta R/R \lesssim 1/\Gamma'$. Notice, however, that this trend is reversed for $\Gamma' \lesssim 2$ (see Fig. 6), which may cause a negative correlation if the typical values of Γ' are in the range: $1 < \Gamma' \lesssim 2$. In Fig. 10, we plot the results for the $L_{\rm max} - V$ correlation for simulated light curves in our model. In calculating the light curve, we assume a typical Band function spectrum emissivity ($\alpha_{\rm B} = 0$, $\beta_{\rm B} = -2.3$) as well as $m = 0$, $k = 0$ and a Gaussian dependence of luminosity on the logarithm of the radius.

We first let $T_{\rm ej}$, Γ' vary between different pulses (according to the distributions assumed in Section 4.6, see Fig. 9). Next, we consider synchrotron emission with a correlation between Γ' and $\gamma'_{\rm e}$ as described in Section 4.5. As mentioned above, such a correlation is less likely to hold for electrons radiating at frequencies corresponding to the sub-MeV peak. However, it still remains an open question whether a similar relation between variability and luminosity also exists at the GeV range. It is therefore important to provide theoretical predictions for this situation which could be tested by observations at a later stage. Again, we let $T_{\rm ej}$ vary randomly for different pulses. We calculate the light curve at a constant observed frequency. As can be seen from equation (34), this means that we should consider $\gamma'_{\rm e}$ = constant between different pulses, implying $K \propto \Gamma'$. We therefore vary K using the same distribution of Γ' as for the case with no correlation. In addition, we assume $k = 1$ for this scenario, as described in Section 4.5. The light curve is then calculated using equation (39). In both cases, we find that for $\sigma_{\ln R} = 0.01$ there is evidence for a positive correlation between $L_{\rm max}$

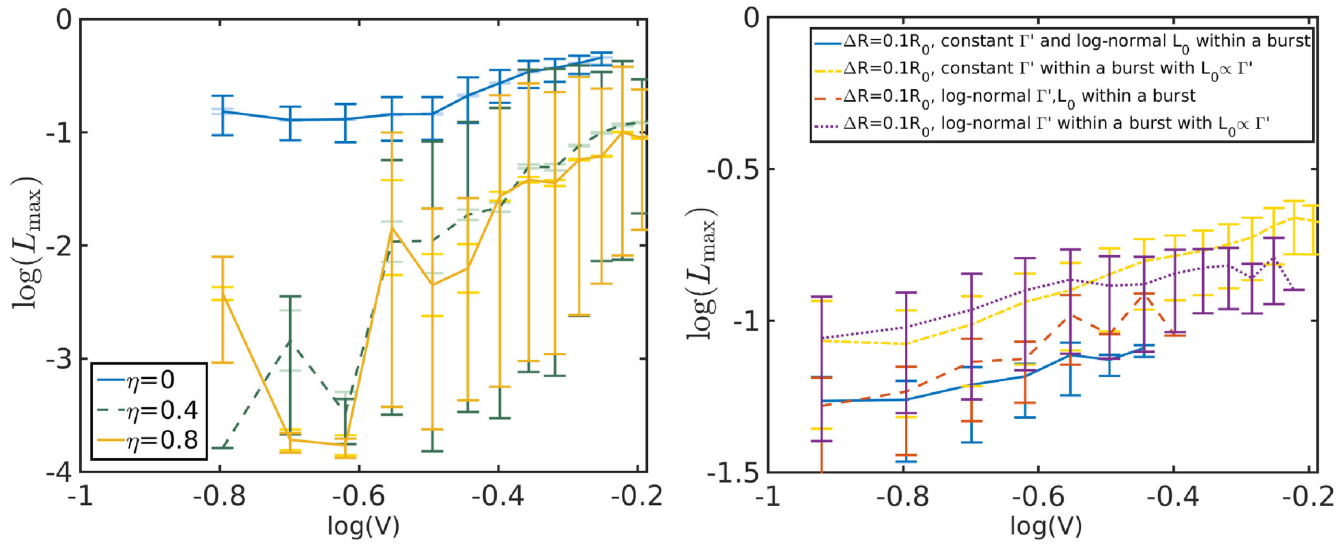

Figure 10. Left: maximal luminosity of a simulated light curve plotted against the variabilities associated with the same light curves using a simplified version of the definition in Reichart et al. (2001) assuming $\Delta R = 0.01R_0$ for a general emission mechanism ($\eta = 0$) and for synchrotron emission with a correlation between Γ' and γ'_e as described in Section 4.5. The inner error bars on each plot are the statistical errors. Notice, that these are small compared with the intrinsic errors, as described in Section 5.1. In the latter, we explore different possibilities for the power-law index of the correlation, η. Right: maximal luminosity as a function of variability for different assumptions on the width of the shells, Γ' (either varying independently between shells or constant within a burst), and the values of F_0 for different pulses (varying lognormally or correlated with Γ').

and V with a power-law index in the range 0.8–4.8 (see left-hand panel of Fig. 10), consistent with the observed values. To quantify the degree of correlation, we calculate the Pearson correlation coefficient for the generated light-curve distributions described above, and find it to be 0.7–0.9. The errors in Fig. 10 denote the smallest range within which lie 68.3 per cent of the values of $\log_{10}(L_{max})$ obtained from different realizations of the light curve. Note that the large errors in Fig. 10 are systematic and not due to insufficient statistics (as is shown explicitly in the left-hand panel of this figure, where we compare the systematic and total errors). They reflect the fact that the variability is set by a combination of many different factors, such as the exact Γ' distribution for the different pulses and whether or not there are overlapping pulses in the light curve. For this reason, a given degree of variability can be obtained by light curves with different intrinsic properties, and different values of L_{max}. Note also that the obtained distribution of L_{max} does not follow a simple lognormal distribution and the errors in general may be asymmetric.

Variation in the dissipation rate and in the associated comoving luminosity over $\Delta R \ll R$ as reflected in $\sigma_{\ln R} = 0.01$ may be present and have some contribution to the overall light curve. However, it is probably more realistic to consider wider shells, or larger $\Delta R/R$. When considering $\sigma_{\ln R} = 0.1$ in the *right-hand panel* of Fig. 10 (and also by letting F_0 vary lognormally, as in Section 4.6, and independently of Γ'), and leaving the other parameters as before, we find that the positive correlation is wiped out. This is because shells with the largest values of Γ' are no longer necessarily the narrowest. In addition, whereas L_{max} depends on the maximal Γ' in the burst, the variability depends on the width of all the pulses in the light curve. Since we have assumed no correlation between Γ' values in different pulses, it is natural that no strong correlation is seen between L_{max} and V.

None the less, reconnection simulations suggest that Γ' increases with the magnetization parameter σ (Guo et al. 2014; Werner et al. 2016), albeit very slowly, and it is not unreasonable that the typical magnetization would vary between different GRBs. Thus motivated, we also explore a simple model in which Γ' varies between different GRBs as in Section 4.6 (i.e. uniformly between 2 and 10) but is constant for a given GRB. We also explore the possibility that $F_0 \propto \Gamma'$. The correlations for these simulated light curves can be seen in the *right-hand panel* of Fig. 10. Even with these modifications, a positive correlation between variability and L_{max}, for shells of width $\Delta R \approx 0.1R_0$ is only obtained when $F_0 \propto \Gamma'$ (resulting in a correlation with a power-law index in the range 0.4–1.2 and a Pearson coefficient of 0.3–0.6). This power-law index is smaller than the observed value of $3.3^{+1.1}_{-0.9}$ reported by Reichart et al. (2001), however it is consistent with the later measurements of $1.3^{+0.8}_{-0.4}$ and 0.8 ± 0.02 found by Guidorzi (2005) and Guidorzi et al. (2005, see discussion above).

5.2 Peak luminosity–peak energy correlation

There have been various claims in the literature that ν_p may be correlated with the peak luminosity, L_p, (Yonetoku et al. 2004; Ghirlanda, Ghisellini & Firmani 2005; Yonetoku et al. 2010). The reported correlations vary in different studies and range between: $L_p \propto \nu_p^{1.5-2}$. We aim to test the viability of such a correlation in the context of our model.

First, recall that:

$$\nu_p \approx \Gamma \nu'_p$$

$$L_p \approx \nu_p L_{\nu_p} \approx (\Gamma \nu'_p)(\Gamma L'_{\nu'_p}) \approx \Gamma^2 L'_p \,. \quad (42)$$

The factor of Γ^2 for the luminosity can be understood as follows. The emitted power in the jet's bulk and observer frames is equal, $dE/dt = dE'/dt'$, but the received power, dE/dT (where T is the observed time), is larger by a factor of $dt/dT = 1/(1-\beta\mu) \sim \Gamma^2$ in the observer frame. This consideration accounts for the angular distribution of the emitted radiation through the estimate $dt/dT \sim \Gamma^2$, which effectively assumes that the observed power is dominated by

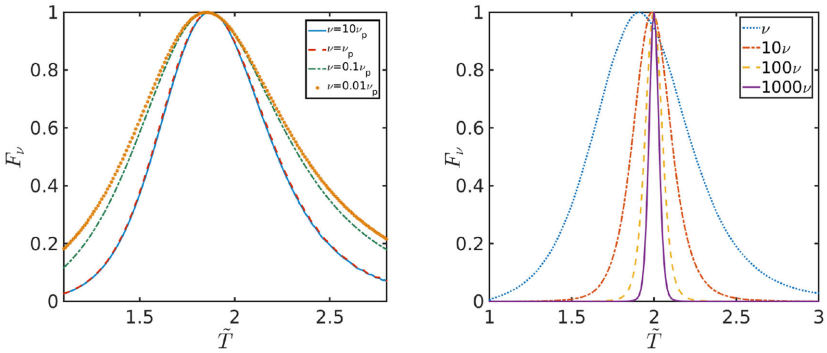

Figure 11. Light curves of a single pulse at different frequencies. All cases are plotted with a typical Band function ($\alpha_B = -1$, $\beta_B = -2.3$), $m = 0$ and a lognormal dependence of luminosity on radius with $\Delta R/R_0 = 0.01$. The maximal flux is normalized to 1, and the time is in units of the typical time T_0 and starting at T_0 (when the first photons reach the observer). Left: no γ'_e–Γ' correlation. In this case, we assume $\Gamma' = 3$, $k = 0$ and a typical Band function. The shape of the peak is roughly constant at different frequencies, but tends to becomes slightly broader below the peak. Right: a γ'_e–Γ' correlation with $\eta = 0.8$, $k = 1$ and with the 'typical' values of Γ' corresponding to the observed frequency (see equation 34), being: 3.4, 8.5, 21.5, 54 from the lowest to highest frequency. In this case, the spectrum is $\nu^{-p/2}$ (see Section 4.5). Here, the pulse clearly becomes narrower with lower frequencies, approximately following the relation $\Delta T \propto \nu^{-0.4}$ implied by equation (34).

material whose radiation is beamed towards the observer. Alternatively, the emitted power per solid angle per particle ($L_{\rm iso,\,e} = {\rm d}E/{\rm d}t{\rm d}\Omega$) scales as $\mathcal{D}^4 \sim \Gamma^4$, but the fraction of the spherical emitting shell size that is within the visible region is $\sim 1/\Gamma^2$ so that together we once more obtain a factor of $\sim\Gamma^2$. Combining the two relations in equation (42), we obtain

$$L_{\rm p} = \left(\frac{\nu_{\rm p}}{\nu'_{\rm p}}\right)^2 L'_{\rm p} \longrightarrow \frac{L_{\rm p}}{\nu_{\rm p}^2} = \frac{L'_{\rm p}}{\nu'^2_{\rm p}}. \tag{43}$$

This implies that if the ratio between the total luminosity in and square of the peak energy in the jet's bulk frame, $L'_{\rm p}/\nu'^2_{\rm p}$, is roughly constant, then a similar relation holds also in the observed frame, $L_{\rm p} \propto \nu_{\rm p}^2$, which reproduces the observed correlation (see also Wijers & Galama 1999; Ghirlanda et al. 2012). This can naturally occur if the properties of the emission are set in the jet's bulk frame. Even more importantly, the result is independent of Γ which is likely to vary significantly from burst to burst (and even within a single burst) and is unlikely to be directly related to the properties of the flow in the comoving frame.

In case of anisotropic emission in the jet's bulk frame, where the emission properties are set in the emitters' frame, as considered in this paper, the situation is more complex. It is most instructive to examine the behaviour for $\Gamma' \gg 1$. From equation (19) that holds for $\Delta R/R_0 > 1/\Gamma'$ (and motivated the definition of $F_0 \propto \Gamma_0\Gamma'^{1-2k}L''_{\nu''_0}$ in equation 26), it can be seen that in this regime $L_{\nu_{\rm p}}/L''_{\nu''_{\rm p}} \sim \Gamma_0\Gamma'^{1-2k}\max(1, R_0/\Delta R)$ where we identify $\nu''_0 \to \nu''_{\rm p} \sim \nu_{\rm p}/\Gamma\Gamma'$ and $L''_{\nu''_0} \to L''_{\nu''_{\rm p}} \sim L''_{\rm p}/\nu''_{\rm p}$. On the other hand, equation (23) that is for a delta function emission in radius and reasonably holds for $\Delta R/R_0 < 1/\Gamma'$ shows that in this regime $L_{\nu_{\rm p}}/L''_{\nu''_{\rm p}} \sim \Gamma_0\Gamma'^{2-2k}$. Since $L_{\rm p}/L''_{\rm p} \sim (\nu''_{\rm p}/\nu_{\rm p})L_{\nu_{\rm p}}/L''_{\nu''_{\rm p}} \sim (L_{\nu_{\rm p}}/L''_{\nu''_{\rm p}})/(\Gamma\Gamma')$, this implies that

$$\frac{L_{\rm p}}{\nu_{\rm p}^2} = \frac{L'_{\rm p}}{\nu'^2} = \frac{L''_{\rm p}}{\nu''^2}\Gamma'^{-2k} f_*\,,$$

$$\times f_* \approx \begin{cases} 1 & \Delta R/R_0 > 1\,, \\ R_0/\Delta R & 1/\Gamma' < \Delta R/R_0 < 1\,, \\ \Gamma' & \Delta R/R_0 < 1/\Gamma'\,. \end{cases} \tag{44}$$

That is, $L''_{\rm p}/\nu''^2_{\rm p} = L_{\rm p}/\nu_{\rm p}^2 \Longleftrightarrow \Gamma'^{-2k} f_* = 1$ is satisfied (i.e. this scaling extends to the emitters' frame) only for $k = 0$ (blob-like emission) and $\Delta R \gtrsim R_0$, but not for $k = 1$ (continuous emission) or $\Delta R < R_0$. In the latter cases, a residual dependence remains on Γ' (for $\Delta R < R_0$), and sometimes also on $\Delta R/R_0$ (for $1/\Gamma' < \Delta R/R_0 < 1$). Nevertheless, it is still reasonable that some of the properties of the emission in the emitters' frame would be determined by processes that occur in the jet's bulk frame, in which the emitters are energized and launched at Γ', so that they could in principle correlate with Γ' and still produce the observed correlations.

We stress that whether or not the ratio $L'_{\rm p}/\nu'^2_{\rm p}$ is indeed constant, depends on the specifics of the emission mechanism, which are not uniquely determined by the model at hand, namely, anisotropic relativistic velocity distribution of particles in the jet's bulk frame. It is none the less intriguing that if such a correlation indeed holds, then it will not be wiped out by variability in Γ (and possibly also in Γ').

5.3 Spectral evolution in a single pulse

Using the results of Section 4.2, we can estimate the typical width of a spike in the light curve at different frequencies. As can be seen in equation (22), so long as there is no γ'_e–Γ' correlation, the width of the pulse is mostly independent of frequency. However, switching between frequencies at different parts of the spectrum (say from the peak to the lower energy spectral slope) can somewhat change the pulse width.

In Fig. 11, we plot the resulting light curve at different frequencies, for a Band spectrum emission. We assume here a typical Band function ($\alpha_B = -1$, $\beta_B = -2.3$), since the intrinsic spectra is model dependent and not uniquely defined by the anisotropic emission model. We note however, that the results presented in this section are not strongly dependent on this assumption, since they are mainly governed by the peak frequency and peak flux which change more as a function of time (as will be shown in Fig. 13). The light curves of a single pulse at four different frequencies compared with the peak: $\nu = 0.01\nu_{\rm p}, 0.1\nu_{\rm p}, \nu_{\rm p}, 10\nu_{\rm p}$. All cases are plotted with $\Gamma' = 3$, $m = 0$ and a Gaussian dependence of luminosity on the logarithm of the radius $\sigma_{\ln R} = 0.01$. For the case with no Γ'–γ'_e correlation, the shape of the peak is roughly constant at different frequencies,

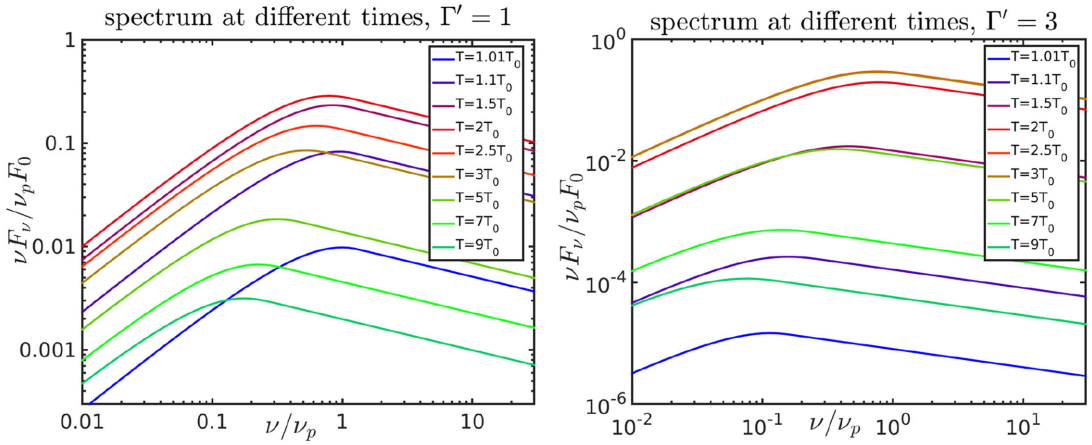

Figure 12. Spectra of a single pulse at nine different times: $T = [1.01, 1.1, 1.5, 2, 2.5, 3, 5, 7, 9]T_0$ for $\Gamma' = 1$ (left) and $\Gamma' = 3$ (right). The intrinsic spectra is assumed to be a typical Band function ($\alpha_B = -1$, $\beta_B = -2.3$) with $m = 0$, $k = 0$ and a constant emissivity from R_0 to $R_f = 2R_0$. The peak of the light curve is at $T = 2T_0$. The spectra is plotted for both $\Gamma' = 1$ (left) and $\Gamma' = 3$ (right). νF_ν is given in the 'typical' units of $\nu_p F_0$ and the frequency is in units of the intrinsic peak frequency ν_p. The spectrum evolves from soft and weak to hard and strong and back again.

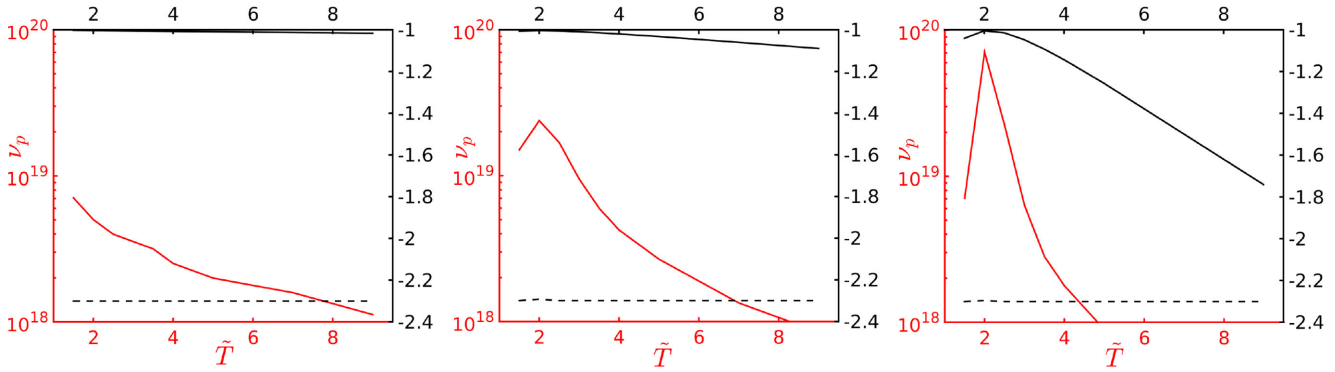

Figure 13. Spectral parameters of a single pulse at different times (left: $\Gamma' = 1$, center: $\Gamma' = 3$, right: $\Gamma' = 10$). The figures are plotted with a constant emissivity from R_0 to $R_f = 2R_0$. The peak frequency is plotted in red and the Band photon indices α_B, β_B are in black (solid and dashed lines accordingly). The intrinsic spectra is assumed to be a typical Band function ($\alpha_B = -1$, $\beta_B = -2.3$) and $m = 0$, $k = 0$. At first the peak energy increases for a short while, and later it decreases significantly. This behaviour is more pronounced for larger values of Γ'. The spectral indexes are basically equal to their intrinsic values and are almost constant in time.

but tends to becomes smoother and somewhat broader at lower frequencies. However, if a correlation between Γ' and γ_e' exists, then higher γ_e' can correspond to a larger ν_{syn} and a larger Γ' and thus a narrower spike, of width (see equation 34) $\Delta T \propto 1/\Gamma' \propto (\nu/\Gamma)^{-\eta/2}$. The observed power-law index of ∼0.4–0.5 (Fenimore et al. 1995; Norris et al. 1996, 2005; Bhat 2012) would suggest $\eta \sim 0.8$–1. However, we stress that due to isotropization of the electrons' orbit due to Larmour gyration, this effect is expected to be mostly dominant near $\nu_{syn,\,max} \approx few \times$GeV, whereas in observations, the pulse widening can be seen at much lower frequencies, down to X-rays.

Another result of this is a change in the spectral shape over time. In Fig. 12, we plot the spectra of a single pulse at nine different times: $T = [1.01, 1.1, 1.5, 2, 2.5, 3, 5, 7, 9]T_0$ for $m = 0$, $k = 0$, a constant dependence of luminosity on radius from R_0 to $R_f = 2R_0$, and for both $\Gamma' = 1$ and 3. The spectrum evolves from soft and weak to hard and strong and back again. Observations of GRB pulses have shown two typical behaviours: intensity tracking and hard to soft evolution (Ford et al. 1995; Preece et al. 2000; Kaneko et al. 2006; Lu et al. 2012). Indeed, Fig. 12 (as well as Figs 13 and 14) demonstrates that our model predicts intensity tracking evolution for sufficiently large Γ' (approximately $\Gamma' > 2$), while a hard to soft evolution appears for low enough Γ' (approximately $\Gamma' < 2$). Since pulses in our model are asymmetric, with the rise time much faster than the decay time, this will make the hard to soft trend much easier to detect than the initial soft to hard (or intensity tracking) evolution, and may account for the observed population of GRB pulses exhibiting 'hard to soft' evolution (for instance this was shown for GRB 130427A in the best analysed pulse to date Preece et al. 2014). Note that a hard to soft evolution is also obtained for $\Gamma' \lesssim 2$. The evolution of the spectral parameters can be seen more directly in Fig. 13 where we plot ν_p and the Band photon indices α_B, β_B as a function of time. The latter do not change significantly in time and remain constant on their intrinsic values. We also note that the change in spectrum becomes significantly more pronounced for as Γ' increases. For the latter, the softening and weakening of the spectrum in time follows the behaviour predicted for regular high-latitude emission: $F_\nu = t^{-2-\alpha}\nu^{-\alpha}$, where α is the relevant spectral slope of F_ν depending on the observed portion of the Band spectrum (either $\alpha = -(\alpha_B + 1)$ or $\alpha = -(\beta_B + 1)$). This behaviour can be seen more clearly in Fig. 14 for $\Gamma' = 1$ and to a lesser extent also for $\Gamma' = 3, 10$ at late times (which would be harder to observe, as the flux is by then much lower than its peak value). Initially, the

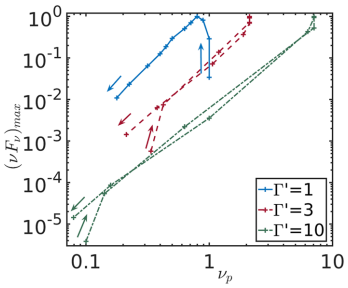

Figure 14. Peak of νF_ν (normalized such that its maximum value is 1) as a function of $\nu_{\rm p}$ (normalized such that the initial peak of the spectrum in the bulk frame is 1) for a single pulse at different times ($\Gamma' = 1$ – solid line, $\Gamma' = 3$ – dashed line and $\Gamma' = 10$ – dash–dotted line). The figures are plotted with a typical Band function ($\alpha_{\rm B} = -1$, $\beta_{\rm B} = -2.3$), $m = 0$, $k = 0$ and a constant emissivity from R_0 to $R_{\rm f} = 2R_0$. Arrows denote the direction of progressing time along the curves. $\Gamma' = 1$ shows a 'hard to soft' behaviour, whereas $\Gamma' = 3$, 10 show an 'intensity tracking behaviour'.

decay for $\Gamma' = 3$ is much steeper and might be able to account for the observed steep decay phase at the beginning of GRB afterglows (e.g. Tagliaferri et al. 2005).

6 DISCUSSION

In this work, we have considered a model for a relativistic source that emits anisotropically in its own bulk rest frame. Our main motivation was to calculate the most prominent expected observational signatures for prompt GRB emission in which the dissipation that powers this emission is driven by magnetic reconnection. This motivated our choice of the geometry of the magnetic reconnection sites (thin spherical shells – reconnection layers) and the bulk Lorentz factor ($\Gamma \gg \Gamma'$). This model may, however, also be applied to other anisotropic emission models in GRBs, as suggested for instance in the relativistic turbulence models and the 'jet in jet' models. This model may also be relevant to other astrophysical systems, such as active galactic nuclei, where very short time-scale variability (minutes) has been discovered (e.g. Aharonian et al. 2007; Albert et al. 2007) possibly suggesting emission from mini-jets within the main relativistic jet (Giannios, Uzdensky & Begelman 2009). Another possible context for relativistic motions in the bulk frame are the GeV flares in the Crab nebula. These flares were suggested to be Doppler boosted emission from the termination shock (Komissarov & Lyutikov 2011) or on the hotspot at the base of the jet feature in the nebulae (Lyubarsky 2012). In both cases, however, the bulk frame is not moving relativistically towards us, but is instead effectively at rest.

We have considered a thin spherical shell propagating at a Lorentz factor $\Gamma \gg 1$, which emits as it expands outwards and either (i) turns on and off abruptly at radii R_0 and $R_{\rm f} = R_0 + \Delta R$, respectively, with the comoving luminosity scaling as a power law (of index a) with radius within this range, or (ii) turns on and off more gradually where the comoving luminosity has a lognormal dependence on radius (centred on R_0 with a standard deviation $\sigma_{\ln R}$). The emitting material is assumed to move at a Lorentz factor Γ' relative to the shell's local rest frame, in a direction transverse to the shell's velocity (i.e. normal to the radial direction). This direction of motion is associated with the antiparallel reconnecting magnetic field lines, and equal amounts of material are assumed to move along the corresponding two opposite directions (e.g. on either side of an x-point within the thin reconnection layer).

Strong magnetic fields may also play an important role in the dynamics of relativistic jets. In AGN jets, the Thompson optical depth at their base is insufficient for efficient thermal acceleration by radiation pressure, suggesting that Blazars' jets must be magnetically accelerated and therefore initially Poynting-flux dominated. In GRBs thermal acceleration is a viable alternative, but hydromagnetic jet launching is expected to dominate, and the required high magnetization near the source helps avoid excessive baryon loading, which might prevent the jet from achieving the required high-Lorentz factors inferred from the GRB prompt emission (for a recent review on the role of magnetic fields in GRBs see Granot et al. 2015). Unconfined steady state, ideal MHD axisymmetric outflows that start highly magnetized (with $\sigma_0 \gg 1$) near the central source remain highly magnetized ($\sigma \sim \sigma_0^{2/3}$) far from the source, while converting only a small fraction of their initial electromagnetic energy to bulk kinetic energy ($\Gamma \sim \sigma_0^{1/3}$). This may be alleviated if the outflow is gradually collimated into a narrow jet of half-opening angle $\theta_{\rm j}$, which could asymptotically lead to $\sigma \sim \sigma_0^{2/3}\theta_{\rm j}^{2/3}$ and $\Gamma \sim \sigma_0^{1/3}\theta_{\rm j}^{-2/3}$, or due to an abrupt drop in the external pressure (e.g. when a long-duration GRB jet breaks out of its progenitor star), but in all cases the asymptotic magnetization is still fairly high, $\sigma \geq 1$. However, the strong Inverse Compton component observed in Blazar spectra suggest a low σ in the emission region (see e.g. Ghisellini & Tavecchio 2009), while in GRBs different lines of evidence suggest a similar conclusion (e.g. Beniamini & Piran 2014). This result is commonly referred to as the σ problem (Goldreich & Julian 1969). This problem may be solved by relaxing one or more of the underlying assumptions of steady state, ideal MHD and axisymmetry. Strong time-dependence can lead to a much more efficient conversion of magnetic to kinetic energy, and to $\sigma < 1$ far from the source that allows efficient dissipation in internal shocks (Granot, Komissarov & Spitkovsky 2011). Alternatively, magnetic reconnection can play an important role in the jet's acceleration and in the reduction of σ, and may be greatly enhanced by various instabilities, some of which or non-axisymmetric (such as the kink instability). The dissipation of magnetic energy generates heat, some of which can be channelled to radiation, but most of which can contribute to the (now thermal) acceleration of the jet. The distance from the central engine where efficient reconnection takes place, will determine whether the jet is still accelerating (Drenkhahn & Spruit 2002; Lyubarsky 2010), coasting, or decelerating (Lyutikov & Blandford 2003; Giannios 2006) at that stage. In GRBs, such late reconnection during the jet's deceleration phase might be expected for the following reason. The jet loses lateral causal contact during its acceleration, eventually reaching $\Gamma\theta_{\rm j} \gg 1$, so that once it starts being decelerated by the external medium increasingly larger angular scales ($\sim 1/\Gamma$) in the jet come into causal contact and allow reconnection of magnetic structures on such scales, which were not possible at earlier times.

Efficient magnetic reconnection may naturally be achieved in a striped wind magnetic field geometry. In this case, the light-curve variability time may reflect the time for the flipping of the magnetic field at the source (i.e. the base of the outflow) over the (dimensionless) comoving flow velocity into the reconnection layer, $\beta'_{\rm in}$. For a magnetar central engine, a periodic flipping of the field's direction is expected with a sign flipping time equal to half of the magnetar's rotational period P, as the local field switches sign twice in each rotation (e.g. Usov 1992). This may lead to relatively 'ordered' light curves with short variability time-scales, $\Delta T \sim 5(P/1\,{\rm ms})(\beta'_{\rm in}/0.1)^{-1}$ ms. These become even shorter for a relativistic inflow velocity $\beta'_{\rm in} \sim 1$ into the reconnection layer that may arise for large σ-values (e.g. Guo et al. 2015), which also

leads to acceleration of the emitters to larger values of Γ'. Such short variability times are typically significantly shorter than the dominant variability time in most GRB light curves.

An alternative option that can naturally lead to larger variability times as observed in most GRB light curves is that the central engine is an accreting black hole, where the magnetic field that is advected inwards with the accreted material randomly switches sign either through some disc instability or by accreting blobs of plasma with a randomly oriented frozen-in magnetic field (e.g. Blandford & Payne 1982; Rees 1984; Uzdensky & MacFadyen 2006; Barkov & Komissarov 2008). In this case, the typical time-scale for a flip in the magnetic field orientation is more uncertain and in addition, due to the stochastic nature of the process, the resulting scale for the flipping of the magnetic field will be much more variable. Therefore, it can potentially account both for the much larger observed typical variability times compared to the naive expectation for a millisecond magnetar, as well as for the large range of variability time-scales that are observed in most GRB light curves and their stochastic nature in general. The resulting efficiency of reconnection in such an outflow with a random flipping of the magnetic field is uncertain, and may be somewhat lower than for a periodic flipping that was mentioned above. This might make it hard to satisfy the high γ-ray emission efficiencies that are commonly inferred from GRB observations (Panaitescu & Kumar 2002; Fan & Piran 2006; Granot et al. 2006). However, as was recently shown by Beniamini et al. (2015) these efficiencies should actually be only moderate ($\sim$0.1), significantly less than what was suggested by some earlier estimates ($\sim$0.9).

Throughout most of this work, we have focused on the properties of the emission that are direct results of anisotropic emission in the jet's bulk frame, and that are largely independent of the specific radiation mechanism/s at work. However, as mentioned above, our main motivation comes from magnetic reconnection models for the energy dissipation. In reconnection models for the prompt emission of GRBs, because of the large expected magnetic fields the most natural radiation mechanism is synchrotron. We consider the emitting electrons to be in the 'slow cooling' regime in order for the spectrum to be consistent with observations in the optical and X-ray bands (Beniamini & Piran 2014). This can be expected if the frame in which the electromagnetic field becomes purely magnetic, is that of the emitters ('the plasmoids'). However, if the latter is in fact the jet's frame, then electrons producing the observed sub-MeV peak will isotropize much faster than they can radiate their energy and the resulting emission would no longer be anisotropic, except at frequencies very close to $\nu_{\rm syn,\,max}$ (see Section 4.5 for details). In 'one zone' magnetically dominated emission regions, the emitting electrons would not be in the 'slow cooling' regime, unless $\Gamma \gtrsim 600$ (Beniamini & Piran 2014); and even then, slow cooling would only occur for the largest possible radii, and mildly relativistic electrons. However, in the anisotropic model, suggested in this paper, there are two important differences compared to the 'one zone' case. First, as mentioned in Section 2 the radius implied by the variability time-scale is larger by a factor Γ' as compared to the non-boosted case (leading to a weaker magnetic field for the same overall luminosity). Secondly, the local magnetic energy density within the reconnection sheet, where the particles are emitting, can be up to an order of magnitude lower than the average field. Combining these two facts implies that in these models, even for a smaller bulk Lorentz factor: $\Gamma \approx 300$, electrons with $\gamma'_{\rm e} \lesssim 10$ will be in the 'slow cooling' regime, as required by both theory and observations. In addition, the upper limit on $\gamma'_{\rm e}$ will increase significantly ($\gamma'_{\rm e} \propto \Gamma^5$) for larger values of Γ.

We briefly summarize our main results and their comparison to the observations:

(i) *Light-curve variability*: GRB light curves show highly variable time profiles with the times between pulses roughly equal to the pulses durations (Nakar & Piran 2002). We show that isotropic reconnection emission models are in conflict with this observation since they generally imply pulse widths significantly broader than the time between pulse peaks. However, we find that the anisotropic emission model presented in this work can produce a highly variable emission at large distances from the central source, as required by observations.

(ii) *Pulse asymmetry*: observed GRB pulses tend to be asymmetric with a typical rise to decay time ratios $t_{\rm rise}/t_{\rm decay} \sim 0.3$–$0.5$ (Nemiroff et al. 1994; Fishman & Meegan 1995; Norris et al. 1996; Quilligan et al. 2002; Hakkila & Preece 2011). Asymmetric pulses with $t_{\rm rise} < t_{\rm decay}$ naturally occur in our model (see Section 4.4 and Table 1) with $t_{\rm rise}/t_{\rm decay}$ depending on the radial dependence of the bulk Lorentz factor ($\Gamma \propto R^{-m/2}$) and comoving luminosity (power law $\propto R^a$ or lognormal $f(R/R_0)$), on Γ', and on the radial extent of the emission producing the pulse, $\Delta R/R_0$. In particular, they naturally occur for $\Delta R \gtrsim R_0$ [e.g. when $f(R/R_0)$ is asymmetric, see for instance the lognormal or power-law functions with $a < 0$, considered in this paper]. Since the shape of a pulse in this case is determined by $f(R/R_0)$, observations of the pulse structure could be used to deduce the evolution of the emissivity powered by magnetic reconnection at a given site in the jet, in a way that may be largely independent of the microphysical properties of the reconnection and instead depend mainly on its gross properties. We note however, that since we effectively see radiation from only a small angular portion of the jet, it would be hard to use this in order to learn about the global structure of the jet. The pulse-shape gradually becomes more symmetric as Γ' increases, so long as $1/\Gamma' > \Delta R/R_0$. At the same limit, the pulse both becomes narrower and peaks at higher fluxes (for a given total radiated energy) for larger Γ'. Finally, we note that for $\Gamma' \gtrsim 2$ and $\Delta R/R_0 \lesssim 1$, the degree of asymmetry depends mainly on $\Delta R/R_0$. Here, once more, observations of the pulse asymmetry could be used to deduce the radial profile of the emission in the jet as mentioned above.

(iii) *Luminosity–variability correlation*: previous studies have found a correlation between the variability of GRB light curves and their peak luminosities (Stern et al. 1999; Fenimore & Ramirez-Ruiz 2000; Reichart et al. 2001; Guidorzi 2005; Guidorzi et al. 2005). For $\Delta R/R \lesssim 1/\Gamma'$ and $\Gamma' \gtrsim 2$ our model predicts that as Γ' increases, the peak luminosities of pulses increase while their widths decrease (leading to larger variabilities). For shells of width $\Delta R/R_0 \lesssim 0.01$ or even (assuming a natural assumption that the luminosities are correlated with Γ') $\Delta R/R_0 \lesssim 0.1$, a correlation between maximal luminosity and the light-curve variability is indeed obtained in our model. Although in the latter case, the power-law index of the correlation is significantly smaller, it is still consistent with the values reported by (Guidorzi et al. 2005) and (Guidorzi 2005).

(iv) $L_{\rm p}$–$\nu_{\rm p}$ *correlation*: many studies have claimed the existence of a correlation between the peak luminosities $L_{\rm p}$ and peak frequencies $\nu_{\rm p}$ of GRBs (Yonetoku et al. 2004; Ghirlanda et al. 2005; Yonetoku et al. 2010) such that $L_{\rm p} \propto \nu_{\rm p}^{1.5-2}$. Recently, it was further suggested (Guiriec et al. 2015) that these results could hold also within a single burst, comparing different pulses. In both the non-boosted ($\Gamma' = 1$) and anisotropic models, both the peak luminosity and peak frequency are Doppler boosted from the emitters' frame. This results in a relation between the luminosity and the

peak frequency in the observer frame that is similar to that in the jet's bulk frame: $\frac{L_p}{\nu_p^2} = \frac{L'_p}{\nu'^2_p}$, independent of the bulk Lorentz factor Γ. This relation implies that if such a correlation between peak frequency and the luminosity exists in the jet's bulk frame, then it would naturally lead to a similar correlation in the observer frame, and would not be wiped out by varying Γ, which is likely to change significantly from burst to burst (and even within a single burst) and is unlikely to be directly related to the properties of the flow in the jet's bulk frame. In case of a blob-like anisotropic emission with $\Delta R/R_0 \gtrsim 1/\Gamma'$ this result can be extended further as it holds also in case the emission properties are set in the emitters' frame.

(v) *Pulse widths and spectral lags*: observations of GRB light curves at different frequencies show that the pulse widths tend to decrease with frequency approximately as $W(\nu) \propto \nu^{-0.4}$ (Fenimore et al. 1995; Norris et al. 1996, 2005; Bhat 2012). A related observation is that at larger frequencies, pulses tend to peak earlier – this is usually referred to as spectral lags (Norris et al. 1996; Band 1997). We note that in case the pulse shape at different frequencies is the same, and the emission starts at the same time, this would follow directly from the anticorrelation between pulse width and frequency mentioned above. In our model, in case there is a correlation between the bulk Lorentz factors of the electrons,γ'_e, and Γ', then it is possible to obtain a negative correlation between the pulse width and the observed frequency, similar to the observed one. This is because higher γ'_e typically correspond to both a larger ν_{syn} and a larger Γ' that leads a narrower spike. The observed relations are reproduced for $\Gamma' \propto \gamma_e'^{0.8-1}$. However, we stress that due to isotropization of the electrons' orbit due to Larmour gyration, this effect is expected to be mostly dominant near $\nu_{syn,\,max} \approx$ *few* $\times$GeV, whereas in observations, the pulse widening can be seen at much lower frequencies, down to X-rays.

(vi) *Single-pulse* L–ν_p *correlation*: observations of GRB pulses have shown two typical behaviours for their evolution in time: *intensity tracking*, where the peak frequency follows the overall flux or luminosity, and *hard to soft* evolution, where the peak frequency is constantly decreasing in time (Ford et al. 1995; Preece et al. 2000; Kaneko et al. 2006; Lu et al. 2012). Interestingly, both behaviours are possible in our model, depending on Γ'. For small anisotropy ($\Gamma' \lesssim 2$), the peak frequency always monotonically decreases, while the flux first increases and later decreases. Therefore, one may expect a 'hard to soft' evolution in this case. However, for larger values of Γ' (>2), the peak frequency also increases at first as the flux rises towards the peak of the pulse, and only later decreases during the tail of the pulse, so in this case one expects an 'intensity tracking' behaviour.

(vii) *Rapid decay phase*: finally, observations of GRBs in the early afterglow phase exhibit a so called 'rapid decay' phase (Tagliaferri et al. 2005). This early phase of rapid flux decay at the end of the prompt emission was unexpected since the flux often falls faster than would be expected from high-latitude emission (which is the shortest time-scale on which the flux can decay, even if the emission shuts off instantly). A possible solution in many cases is that the initial fast decay is dominated by the last pulse so that the zero-point for the power-law decay should be taken as the onset of that last pulse rather than of the whole GRB, i.e. the onset of the first pulse. In the anisotropic model, the initial flux decay of a single pulse is significantly more rapid than in the non-boosted case (and increases with Γ'), and is thus able to account even for the most extreme cases of such rapid decay phases. A similar solution, producing rapid decays due to anisotropic emission was considered by Beloborodov et al. (2011) who suggested an anisotropic emission model for GRB afterglows.

We conclude that the simple anisotropic emission model presented in this paper is able to reproduce many of the observational features seen in the prompt emission of GRBs, and therefore seems very promising. In a future work, we plan to extend this model to more realistic magnetic reconnection configurations, such as those obtained in relativistic reconnection simulations. This would help determine some of the free parameters that still exist in this model and could provide a self-consistent model for energy dissipation and emission in the prompt phase of GRBs.

ACKNOWLEDGEMENTS

We thank Tsvi Piran, Daniel Kagan, Pawan Kumar and Wenbin Lu for helpful discussions. We also thank the anonymous referee for helpful suggestions and comments. This research was supported in part by the ISF grant 719/14 (JG).

REFERENCES

Abdo A. A. et al., 2009a, Science, 323, 1688
Abdo A. A. et al., 2009b, ApJ, 707, 580
Ackermann M. et al., 2010, ApJ, 716, 1178
Aharonian F. et al., 2007, ApJ, 664, L71
Albert J. et al., 2007, ApJ, 669, 862
Asano K., Terasawa T., 2015, MNRAS, 454, 2242
Band D. L., 1997, ApJ, 486, 928
Barkov M. V., Komissarov S. S., 2008, MNRAS, 385, L28
Beloborodov A. M., Daigne F., Mochkovitch R., Uhm Z. L., 2011, MNRAS, 410, 2422
Beniamini P., Piran T., 2013, ApJ, 769, 69
Beniamini P., Piran T., 2014, MNRAS, 445, 3892
Beniamini P., Lara N., Barniol Duran R., Piran T., 2015, MNRAS, 454, 1073
Bhat P. N. et al., 2012, ApJ, 744, 141
Blandford R. D., Payne D. G., 1982, MNRAS, 199, 883
Cerutti B., Werner G. R., Uzdensky D. A., Begelman M. C., 2012, ApJ, 754, L33
Cerutti B., Werner G. R., Uzdensky D. A., Begelman M. C., 2013, ApJ., 770, 147
Coroniti F. V., 1990 ApJ 349, 538
Daigne F., Bosnjak Z., Dubus G., 2011, A&A, 526, 110
de Jager O. C., Harding A. K., Michelson P. F., Nel H. I., Nolan P. L., Sreekumar P., Thompson D. J., 1996, ApJ, 457, 253
Drenkhahn G., Spruit H. C., 2002, A&A, 391, 1141
East W. E., Zrake J., Yuan Y., Blandford R. D., 2015, Phys. Rev. Lett., 115, 095002
Fan Y. Z., 2010, MNRAS, 403, 483
Fan Y. Z., Piran T., 2006, MNRAS, 369, 197
Fenimore E. E., Ramirez-Ruiz E., 2000, preprint (astro-ph/0004176)
Fenimore E. E., in't Zand J. J. M., Norris J. P., Bonnell J. T., Nemiroff R. J., 1995, ApJ, 448, L101
Fishman G. J., Meegan C. A., 1995, ARA&A, 33, 415
Ford L. A. et al., 1995, ApJ, 439, 307
Frail D. A. et al., 2000, ApJ, 538, L129
Genet F., Granot J., 2009, MNRAS, 399, 1328
Ghirlanda G., Celotti A., Ghisellini G., 2002, A&A, 393, 409
Ghirlanda G., Ghisellini G., Firmani C., 2005, MNRAS, 361, L10
Ghirlanda G., Nava L., Ghisellini G., Celotti A., Burlon D., Covino S., Melandri A., 2012, MNRAS, 420, 483
Ghisellini G., Celotti A., 1999, ApJ, 511, L93
Ghisellini G., Tavecchio F., 2009, MNRAS, 397, 985
Giannios D., 2006, A&A, 455, L5
Giannios D., Uzdensky D. A., Begelman M. C., 2009, MNRAS, 395, L29
Goldreich P., Julian W. H., 1969, ApJ, 157, 869

Granot J., 2005, ApJ, 631, 1022
Granot J., Königl A., 2003, ApJ, 594, L83
Granot J., Panaitescu A., Kumar P., Woosley S. E., 2002, ApJ, 570, L61
Granot J., Ramirez-Ruiz E., Perna R., 2005, ApJ, 630, 1003
Granot J., Konigl A., Piran T., 2006, MNRAS, 370, 1946
Granot J., Cohen-Tanugi J., do Couto e Silva E., 2008, ApJ, 677, 92
Granot J., Komissarov S. S., Spitkovsky A., 2011, MNRAS, 411, 1323
Granot J., Piran T., Bromberg O, Racusin J. L., Daigne F., 2015, in Balogh A. et al., eds, Space Science Series of ISSI, The Strongest Magnetic Fields in the Universe, Volume 54. Springer-Verlag, Berlin, p. 471
Guidorzi C., 2005, MNRAS, 364, 163
Guidorzi C., Frontera F., Montanari E., Rossi F., Amati L., Gomboc A., Hurley K., Mundell C. G., 2005, MNRAS, 363, 315
Guidorzi C., Frontera F., Montanari E., Rossi F., Amati L., Gomboc A., Mundell C. G., 2006, MNRAS, 371, 843
Guiriec S. et al., 2012, 39th COSPAR Scientific Assembly, 39, 682G
Guiriec S. et al., 2015, ApJ, 807, 148
Guo F., Li H., Daughton W., Liu Y.-H., 2014, Phys. Rev. Lett., 113, 155005
Guo F., Liu Y. H., Daughton W., Li H., 2015, ApJ, 806, 167
Hakkila J., Preece R. D., 2011, ApJ, 740, 104
Inoue T., Asano K., Ioka K., 2011, ApJ, 734, 77
Kagan D., Sironi L., Cerutti B., Giannios D., 2015, Space Sci. Rev., 191, 545
Kaneko Y., Preece R. D., Briggs M. S., Paciesas W. S., Meegan C. A., Band D. L., 2006, ApJS, 166, 298
Katz J. I., 1994, ApJ, 422, 248
Kawanaka N., Piran T., Krolik J. H., 2013, ApJ, 766, 31
Kobayashi S., Ryde F., MacFadyen A., 2002, ApJ, 577, 302
Komissarov S. S., Lyutikov M., 2011, MNRAS, 414, 2011
Kumar P., Crumley P., 2015, MNRAS, 453, 1820
Kumar P., McMahon E., 2008, MNRAS, 384, 33
Kumar P., Narayan R., 2009, MNRAS, 395, 472
Lazar A., Nakar E., Piran T., 2009, ApJ, 695, L10
Lazarian A., Kowal G., Takamoto M., de Gouveia Dal Pino E. M., Cho J., 2015, in Gonzalez W., Parker E. N., eds, Astrophysics and Space Science Library, Vol. 427, Magnetic Reconnection. Springer International Publishing, Switzerland, p. 409
Levinson A., Eichler D., 1993, ApJ, 418, 386
Liu Y.-H., Guo F., Daughton W., Li H., Hesse M., 2015, Phys. Rev. Lett., 114, 095002
Lu R.-J., Wei J.-J., Liang E.-W., Zhang B.-B., Lü H.-J., Lü L.-Z., Lei W.-H., Zhang B., 2012, ApJ, 756, 112
Lyubarsky Y. E., 2005, MNRAS, 358, 113
Lyubarsky Y. E., 2010, ApJ, 725, 234L
Lyubarsky Y. E., 2012, MNRAS, 427, 1497
Lyutikov M., Blandford R., 2003, preprint (astro-ph/0312347)
Melzani M., Walder R., Folini D., Winisdoerffer C., Favre J. M., 2014, A&A, 570, 112
Mészáros P., Rees M. J., 1997, ApJ, 482, L29
Murase K., Asano K., Terasawa T., Mészáros P., 2012, ApJ, 746, 164
Nakar E., Piran T., 2002, MNRAS, 331, 40
Nava L., Ghirlanda G., Ghisellini G., Celotti A., 2011, A&A, 530, A21
Nemiroff R. J., Norris J. P., Kouveliotou C., Fishman G. J., Meegan C. A., Paciesas W. S., 1994, ApJ, 423, 432
Norris J. P., Nemiroff R. J., Bonnell J. T., Scargle J. D., Kouveliotou C., Paciesas W. S., Meegan C. A., Fishman G. J., 1996, ApJ, 459, 393
Norris J. P., Bonnell J. T., Kazanas D., Scargle J. D., Hakkila J., Giblin T. W., 2005, ApJ, 627, 324
Panaitescu A., Kumar P., 2002, ApJ, 571, 779
Pedersen H. et al., 1998a, ApJ, 496, 311
Preece R. D., Briggs M. S., Mallozzi R. S., Pendleton G. N., Paciesas W. S., Band D. L., 1998b, ApJ, 506, 23
Preece R. D., Briggs M. S., Mallozzi R. S., Pendleton G. N., Paciesas W. S., Band D. L., 2000, ApJS, 126, 19
Preece R. et al., 2014, Science, 343, 51
Quilligan F., McBreen B., Hanlon L., McBreen S., Hurley K. J., Watson D., 2002, A&A, 385, 377
Rees M. J., 1984, ARA&A, 22, 471
Rees M. J., Mészáros P., 1994, ApJ, 430, L93
Reichart D. E., Lamb D. Q., Fenimore E. E., Ramirez-Ruiz E., Cline T. L., Hurley K., 2001, ApJ, 552, 57
Sari R., Narayan R., Piran T., 1996, ApJ, 473, 204
Sari R., Piran T., Narayan R., 1998, ApJ, 497, L17
Shemi A., Piran T., 1990, ApJ, 365, L55
Sironi L., Spitkovsky A., 2014, ApJ, 783, L21
Sironi L., Petropoulou M., Giannios D., 2015, MNRAS, 450, 183
Spruit H. C., 1999, A&A, 341, L1
Stern B., Poutanen J., Svensson R., 1999, ApJ, 510, 312
Tagliaferri G. et al., 2005, Nature, 436, 985
Thompson C., 1994, MNRAS, 270, 480
Usov V. V., 1992, Nature, 357, 472
Uzdensky D. A., MacFadyen A. I., 2006, ApJ, 647, 1192
Werner G. R., Uzdensky D. A., Cerutti B., Nalewajko K., Begelman M. C., 2016, ApJ, 816, L8
Wijers R. A. M. J., Galama T. J., 1999, ApJ, 523, 177
Yonetoku D., Murakami T., Nakamura T., Yamazaki R., Inoue A. K., Ioka K., 2004, ApJ, 609, 935
Yonetoku D., Murakami T., Tsutsui R., Nakamura T., Morihara Y., Takahashi K., 2010, PASJ, 62, 1495
Zrake J., 2014, ApJ, 794, L26
Zrake J., 2015, preprint (arXiv:1512.05426)
Zrake J., East W. E., 2016, ApJ, 817, 89

APPENDIX A: APPROXIMATE EXPRESSION FOR THE FLUX

Here, we derive the result in equation (19), by solving the double-integral in equation (18) in the limit $\Gamma' \gg 1$. First, the inner integral, may be written as

$$I_1 = \int_0^{2\pi} \mathrm{d}\phi (1 - \beta' \sin\theta' \cos\phi)^{k-\alpha-3} . \quad \text{(A1)}$$

Since the power $k - \alpha - 3$ is typically negative, the integrand becomes maximal when $(1 - \beta' \sin\theta' \cos\phi)$ is minimal, i.e. for $\phi = 0$, $\theta' = \pi/2$, and it rapidly drops for different values of ϕ, θ'. Therefore, in order to evaluate the inner integral we can use the approximation $\phi \ll 1$ and $\cos\phi \approx 1 - \phi^2/2$, and take the limits of integration to be form $-\infty$ to ∞ (as the dominant contribution is anyway from a small region where $|\phi| \lesssim 1/\Gamma' \ll 1$),

$$I_1 \approx \int_{-\infty}^{\infty} \mathrm{d}\phi \left[1 - \beta' \sin\theta' \left(1 - \frac{\phi^2}{2}\right)\right]^{k-\alpha-3}$$
$$= \frac{\sqrt{2\pi}\,\Gamma(2.5 + \alpha - k)}{\Gamma(3 + \alpha - k)} \frac{(1 - \beta' \sin\theta')^{k-\alpha-2.5}}{\sqrt{\beta' \sin\theta'}} , \quad \text{(A2)}$$

where here Γ is the γ function. As for the outer integration, over y, since most of the contribution is from $\theta' \approx \pi/2$, this corresponds to $y \approx y_0 = (m + 2)^{-1/(m+1)}$, so that

$$\left(\frac{m+1}{m + y^{-m-1}}\right)^{2+\alpha} y^{a-1-m/2(1+\alpha)}$$
$$\approx 2^{-2-\alpha} (m + 2)^{m(1+\alpha)+2(1-a)/2(m+1)} . \quad \text{(A3)}$$

Also, the integral does not vanish only if the corresponding radius, $R = yR_{\rm L} \approx y_0 R_{\rm L} = y_0 R_0 (T/T_0)^{1/(m+1)}$ is in the emission region, i.e. between R_0 and $R_{\rm f}$, or

$$1 < \left[\frac{T}{(m+2)T_0}\right]^{1/m+1} < \frac{R_{\rm f}}{R_0} . \quad \text{(A4)}$$

Moreover, $\sqrt{\beta' \sin\theta'} \approx 1$, so that the only term in the integrand that significantly varies in the region where the dominant contribution

comes from is $(1-\beta'\sin\theta')^{k-\alpha-2.5}$. Now we can define $\tilde{y} = y - y_0 \ll 1$ and approximate

$$\sin\theta' = 2\frac{\sqrt{(m+1)(y^{-m-1}-1)}}{m+y^{-m-1}} \approx 1 - \frac{\tilde{y}^2}{8y_0^{2(m+2)}}\,. \tag{A5}$$

Taking also the limit where $\Gamma' \gg 1$ so that $\beta' \approx 1 - 1/2\Gamma'^2$, we have

$$(1-\beta'\sin\theta')^{k-\alpha-2.5} \approx \left(\frac{1+\frac{1}{4}\Gamma'^2\tilde{y}^2 y_0^{-2(m+2)}}{2\Gamma'^2}\right)^{k-\alpha-2.5}\,. \tag{A6}$$

Changing variables to $\bar{y} = \tilde{y}\Gamma'/2y_0^{m+2}$, we have $\mathrm{d}y = \mathrm{d}\tilde{y} = (2y_0^{m+2}/\Gamma')\mathrm{d}\bar{y}$. Since the main contribution to the integral is from $\bar{y}$ of order unity, then for $\Gamma' \gg 1$ we can take the limits of integration over $\bar{y}$ form $-\infty$ to ∞, and when the condition in equation (A4) is satisfied one obtains

$$\begin{aligned}
&\int_{y_{\min}}^{y_{\max}} \mathrm{d}y(1-\beta'\sin\theta')^{k-\alpha-2.5} \\
&\quad\approx \Gamma'^{4+2\alpha-2k}2^{3.5+\alpha-k}y_0^{m+2}\int_{-\infty}^{\infty}\mathrm{d}\bar{y}(1+\bar{y}^2)^{k-\alpha-2.5} \\
&\quad= \Gamma'^{4+2\alpha-2k}2^{3.5+\alpha-k}y_0^{m+2}\frac{\sqrt{\pi}\,\Gamma(2+\alpha-k)}{\Gamma(2.5+\alpha-k)}\,.
\end{aligned} \tag{A7}$$

Putting all the terms together we obtain

$$\begin{aligned}
F_\nu(T) \approx\ & \frac{\Gamma_0\Gamma'^{1-2k}L''_{\nu_0''}}{2^k\pi D^2}\left(\frac{\nu}{\nu_0}\right)^{-\alpha}\left(\frac{T}{T_0}\right)^{2a-m(1+\alpha)/2(m+1)} \\
&\times\frac{(a+1)(m+2)^{m(\alpha-1)-2(a+1)/2(m+1)}}{\left(1+\frac{\Delta R}{R_0}\right)^{a+1}-1}\frac{\Gamma(2+\alpha-k)}{\Gamma(3+\alpha-k)}\,.
\end{aligned} \tag{A8}$$

APPENDIX B: ANGULAR TIME-SCALE IN THE ANISOTROPIC EMISSION MODEL

We aim to find here the angular time-scale for the model with anisotropic emission presented in this paper and show that it is $T_\theta = (1+z)R/c\Gamma^2\Gamma'$. We define $\xi = (\Gamma\theta)^2$. In the relativistic limit, $\Gamma \gg 1$, the main contribution to the radiation comes from $\theta \ll 1$ for which $\cos\theta \approx 1 - \theta^2/2$, and $\beta = v/c \approx 1 - 1/2\Gamma^2$ so that

$$\begin{aligned}
R &= \int_0^t \beta(t')c\mathrm{d}t' \approx ct - \int_0^R \frac{\mathrm{d}R'}{2\Gamma^2(R')} = ct - \frac{R}{2(m+1)\Gamma^2(R)} \\
&\implies\quad t \approx \frac{R}{c}\left[1+\frac{1}{2(m+1)\Gamma^2}\right]\,.
\end{aligned} \tag{B1}$$

Using the definition of the EATS along with the relations $R/R_0 = y(T/T_0)^{1/(m+1)}$ and $R/\Gamma^2 = (R/R_0)^{m+1}R_0/\Gamma_0^2 = y^{m+1}(T/T_0)R_0/\Gamma_0^2$ (see equations 9 and 10) one obtains

$$\begin{aligned}
T &= (1+z)\left[t - \frac{R\cos\theta}{c}\right] \approx \frac{(1+z)R}{2(m+1)c\Gamma^2}\left[1+(m+1)\xi^2\right] \\
&= Ty^{m+1}\left[1+(m+1)\xi^2\right]\,.
\end{aligned} \tag{B2}$$

This can be inverted to obtain an expression for ξ (see for instance Genet & Granot 2009):

$$\xi = (\Gamma\theta)^2 = \frac{y^{-m-1}-1}{m+1} \quad\Longleftrightarrow\quad y^{-m-1} = 1+(m+1)\xi\,. \tag{B3}$$

Plugging this into the expression for $\sin\theta'$ (equation 12) we obtain

$$\sin^2\theta' = \frac{4(m+1)(y^{-m-1}-1)}{(m+y^{-m-1})^2} = \frac{4\xi}{(1+\xi)^2}\,. \tag{B4}$$

Let us also define the angle between $\hat{n}'$ and $\hat{\beta}'$ as χ'. By definition, and using the fact that $\cos^2\phi = \cos^2\phi'$, we have

$$\cos^2\chi' = (\hat{n}'\cdot\hat{\beta}')^2 = \sin^2\theta'\cos^2\phi' = \frac{4\xi}{(1+\xi)^2}\cos^2\phi\,. \tag{B5}$$

Defining the parameter

$$f = \frac{\cos^2\phi}{\cos^2\chi'}\,, \tag{B6}$$

we thus obtain a quadratic equation for ξ,

$$4f\xi = (1+\xi)^2 \quad\Longrightarrow\quad \xi^2 + \xi(2-4f)+1 = 0\,, \tag{B7}$$

for which the solutions are

$$\xi_\pm = 2f - 1 \pm \sqrt{(2f-1)^2-1}\,. \tag{B8}$$

The dominant contribution to the emission arises from within the beaming cone, i.e. from $\chi' \le 1/\Gamma'$. Therefore, in order to find the boundaries of this region, we simply substitute $\chi' = 1/\Gamma'$ in the expression for the parameter f in equation (B6). Hence, each value of f corresponds to a particular value of $\cos^2\phi$, which in turn correspond to four different values of $\phi = \pm\phi_0$ and $\pi \pm \phi_0$. For each of these ϕ values, there are two values of $\xi = \xi_\pm$ according to equation (B8), which each correspond to a value of θ. As shown in Fig. 5, for a given value of Γ' this implies two approximately circular regions of angular radius $\approx 1/(\Gamma'\Gamma)$ around the two points of intersection of the x'-axis ($\phi = 0, \pi$) with the circle of angular radius $\theta = 1/\Gamma$ around the line of sight (i.e. $\xi = 1$), i.e. $(\xi,\phi) = (1,0)$ and $(1,\pi)$ or $(\theta,\phi) = (1/\Gamma, 0)$ and $(1/\Gamma,\pi)$. For a given value of $\chi' = 1/\Gamma'$, there are solutions for ξ only for f in the range $1 \le f \le 1/\cos^2\chi'$. The outer edges of this regions in the ϕ direction correspond to $f = 1$ and $\phi_0 = \chi' = 1/\Gamma'$. The corresponding angular separation or distance from the centre of the relevant region is $\approx\phi_0/\Gamma = 1/(\Gamma'\Gamma)$. Along the x'-axis $\phi_0 = 0$, $f = 1/\cos^2\chi' = 1/\cos^2(1/\Gamma') \approx 1 + 1/\Gamma'^2$ or $2f - 1 \approx 1 + 2/\Gamma'^2$, where the last approximation holds for $\Gamma' \gg 1$, for which in this case one obtains

$$\xi_\pm \approx 1 + \frac{2}{\Gamma'^2} \pm \sqrt{\left(1+\frac{2}{\Gamma'^2}\right)^2 - 1} \approx 1 \pm \frac{2}{\Gamma'}\,, \tag{B9}$$

for which the corresponding values of θ are

$$\Gamma\theta_\pm = \sqrt{1\pm\frac{2}{\Gamma'}} \approx 1 \pm \frac{1}{\Gamma'} \quad\Longrightarrow\quad \theta_\pm \approx \frac{1}{\Gamma} \pm \frac{1}{\Gamma\Gamma'}\,, \tag{B10}$$

which again correspond to an angular separation or distance from the centre of the relevant region (that corresponds to $\theta = 1/\Gamma$ with the same value of $\phi = 0$ or π) of $\approx\phi_0/\Gamma = 1/(\Gamma'\Gamma)$.

We see that the typical range of θ from which a dominant contribution to the emission arrives is indeed $1/(\Gamma\Gamma')$. We can now estimate the angular time-scale, which is the difference in arrival times of photons from $\theta_1 = 1/\Gamma$ and $\theta_2 = 1/\Gamma + 1/(\Gamma\Gamma')$:

$$\begin{aligned}
\frac{T_\theta}{1+z} &= \frac{R}{c}(\cos\theta_- - \cos\theta_+) \approx \frac{R}{c}\left(\frac{\theta_+^2}{2} - \frac{\theta_-^2}{2}\right) \\
&= \frac{R}{2c}(\theta_+ + \theta_-)(\theta_+ - \theta_-) \approx \frac{2R}{c\Gamma^2\Gamma'}\,.
\end{aligned} \tag{B11}$$

This is taking the diameter of this approximately circular region. A better estimate is obtained by using its angular radius, which results a time smaller by a factor of 2,

$$T_\theta \approx \frac{(1+z)R}{c\Gamma^2\Gamma'}\,, \tag{B12}$$

that is shorter by a factor $\Gamma'/2$ than the angular time for the case of non-boosted emission in the jet's bulk frame.

APPENDIX C: THE TYPICAL ELECTRONS' ENERGY IN THE EMITTERS' FRAME

Consider a distribution of electrons, such that for a given γ_e', electrons velocities are distributed uniformly within a cone of half-opening angle $\theta_0(\gamma_e')$ around the x'-axis in the jet's bulk frame. The four velocity of an electron with a random Lorentz factor γ_e' travelling at some angle $\tilde{\theta}$ to the x'-axis in the jet's bulk frame, is given by

$$u^{\mu} = (\gamma_e', \gamma_e'\beta_e\tilde{\mu}, \gamma_e'\beta_e\sqrt{1-\tilde{\mu}^2}, 0), \tag{C1}$$

where $\beta_e = \sqrt{1-\gamma_e'^{-2}}$ and $\tilde{\mu} = \cos\tilde{\theta}$. Transforming this expression to the emitters' frame, moving at $\Gamma' = (1-\beta'^2)^{-1/2}$ in the x'-direction in the jet's bulk frame (notice that Γ' can be a function of γ_e'), we obtain

$$u'^{\mu} = (\Gamma'\gamma_e'(1-\beta'\beta_e\tilde{\mu}), \Gamma'\gamma_e'(\beta_e\tilde{\mu}-\beta'), \gamma_e'\beta_e\sqrt{1-\tilde{\mu}^2}, 0). \tag{C2}$$

The average momentum in the x' direction should be zero in the emitters' frame, as it may be defined as the particles' local CM frame. This implies that

$$\begin{aligned} 0 &= \langle u'^1\rangle = \langle\Gamma'\gamma_e'(\beta_e\tilde{\mu}-\beta')\rangle \\ &= \Gamma'\gamma_e'(\beta_e\langle\tilde{\mu}\rangle-\beta') \quad\Longrightarrow\quad \beta' = \beta_e\langle\tilde{\mu}\rangle\,. \end{aligned} \tag{C3}$$

The average $\langle\tilde{\mu}\rangle$ can be written in terms of θ_0 or $\mu_0 = \cos\theta_0 \approx 1-\frac{1}{2}\theta_0^2$:

$$\langle\tilde{\mu}\rangle = \frac{1}{1-\mu_0}\int_{\mu_0}^{1}\tilde{\mu}d\tilde{\mu} = \frac{1+\mu_0}{2} \approx 1-\frac{\theta_0^2}{4}\,. \tag{C4}$$

Note that $\tilde{\theta}_{\langle\tilde{\mu}\rangle} \equiv \arccos\langle\tilde{\mu}\rangle \approx \theta_0/\sqrt{2}$ differs from $\langle\tilde{\theta}\rangle = (\theta_0\cos\theta_0 - \sin\theta_0)/(1-\cos\theta_0) \approx \frac{2}{3}\theta_0$. Given β' from equation (C3) in terms of the average properties, we can also obtain Γ'

$$\begin{aligned} \Gamma' &= \frac{1}{\sqrt{1-\beta_e^2\langle\tilde{\mu}\rangle^2}} = \frac{1}{\sqrt{1-\beta_e^2(\frac{1+\mu_0}{2})^2}} \\ &\approx \frac{\gamma_e'}{\sqrt{1+\frac{(\gamma_e'\theta_0)^2}{2}}} = \begin{cases} \gamma_e' & \gamma_e'\theta_0 \ll 1, \\ \frac{\sqrt{2}}{\theta_0} & \gamma_e'\theta_0 \gg 1\,. \end{cases} \end{aligned} \tag{C5}$$

Plugging this back into the zeroth coordinate of the four velocity in the emitters' frame we get that the average energy of particles in this frame is given by

$$\gamma_e'' \equiv \langle u'^0\rangle = \Gamma'\gamma_e'(1-\beta_e^2\langle\tilde{\mu}\rangle^2) = \frac{\gamma_e'}{\Gamma'} \tag{C6}$$

as given by equation (33).

This paper has been typeset from a TEX/LATEX file prepared by the author.